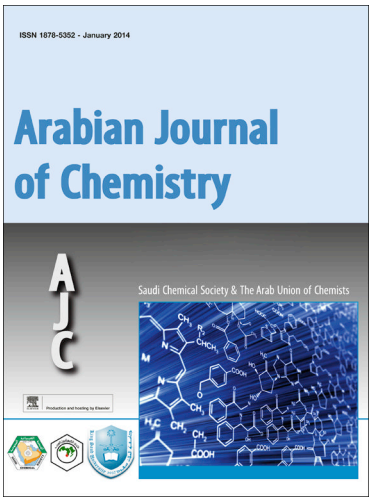

Original article

Facile LaOF: Sm^{3+} based labeling agent and their applications in residue chemistry of latent fingerprint and cheiloscopy under UV-visible light

C. Suresh, H. Nagabhushana, G.P. Darshan, R.B. Basavaraj, D. Kavyashree, S.C. Sharma, A. Arulmozhi, B. Daruka Prasad, H.J. Amith Yadav

PII: S1878-5352(17)30183-1
DOI: https://doi.org/10.1016/j.arabjc.2017.09.014
Reference: ARABJC 2155

To appear in: *Arabian Journal of Chemistry*

Received Date: 21 June 2017
Accepted Date: 25 September 2017

Please cite this article as: C. Suresh, H. Nagabhushana, G.P. Darshan, R.B. Basavaraj, D. Kavyashree, S.C. Sharma, A. Arulmozhi, B. Daruka Prasad, H.J. Amith Yadav, Facile LaOF: Sm^{3+} based labeling agent and their applications in residue chemistry of latent fingerprint and cheiloscopy under UV-visible light, *Arabian Journal of Chemistry* (2017), doi: https://doi.org/10.1016/j.arabjc.2017.09.014

Facile LaOF: Sm^{3+} based labeling agent and their applications in residue chemistry of latent fingerprint and cheiloscopy under UV-visible light

C. Suresh[1, 2], H. Nagabhushana[1, *], G. P. Darshan[3], R.B. Basavaraj[1], D. Kavyashree[4], S.C. Sharma[5, 6], A. Arulmozhi[7], B. Daruka Prasad[8], H.J. Amith Yadav[9]

[1]Prof. C.N.R. Rao Centre for Advanced Materials, Tumkur University, Tumkur 572 103, India
[2]Department of Physics, Govt. First Grade College, Tumkur 572 103, India
[3]Department of Physics, Acharya Institute of Graduate Studies, Bangalore 560 107, India
[4]Department of Physics, Channabasaveshwara Institute of Technology, VTU affiliated, Gubbi 572 216, India
[5]Advisor, Avinashilingam Institute for Home Science and Higher Education for Women University, Coimbatore 641 043, India
[6]Department of Mechanical Engineering, Jain University, Advisor, Jain group of Institutions, Bangalore 560 069, India
[7]Department of Printing technology, Avinashilingam Institute for Home Science and Higher Education for Women University, Coimbatore 641 043, India
[8]Department of Physics, BMS Institute of Technology and Management, VTU-affiliated, Bangalore 560 064, India
[9]Department of Physics, Bangalore University, Bangalore -560056, India

* Corresponding author: E-mail: bhushanvlc@gmail.com (H. Nagabhushana).

Abstract

Luminescent lanthanum oxyfluoride nano inorganic materials were considered to be prospective building blocks for multifunctional applications. This offers new potentials in surface-based science comprising of visualization of latent fingerprint (LFPs) and lips print on non-porous surfaces. Traditional visualization techniques possess high backward hindrance, low sensitivity, complicated setup and poor visibility. To overcome with these problems, LaOF: Sm^{3+} (5 mol %) nanopowder (NPsS) prepared via sonochemical route were explored. Photoluminescence (PL) emission spectra exhibit strong emission peaks at ~ 566 nm, 607 nm, 653 nm and 708 nm attributed to $^4G_{5/2} \rightarrow {}^6H_{5/2}$, $^4G_{5/2} \rightarrow {}^4H_{7/2}$, $^4G_{5/2} \rightarrow {}^6H_{9/2}$ and $^4G_{5/2} \rightarrow {}^6H_{11/2}$ intra-4f orbital transitions of Sm^{3+} ions respectively. Estimated photometric properties confirm that the material emits warm orange red color. Therefore, the synthesized phosphor materials may quite useful for LFPs recovery, cheiloscopy and optoelectronics applications.

Keywords: Ultrasonication; Photoluminescence; Forensic; Cheiloscopy; Solid state lighting.

1. Introduction

Fingerprints (FPs) were universal investigative protocol for the identification of individuals and imparting added records of the individuals in forensic field. Certain FPs can be visualized without hindrance, when the fingers were stained with extrinsic additives including, blood, food contaminants, paint, moisture etc. Such FPs was referred to as latent fingerprints (LFPs). Nevertheless, the majority of FPs on many surfaces have been due to sweat accommodates with the help of epidermis, secretory glands (eccrine, apocrine, apoeccrine and sebaceous) etc. These FPs were invisible to bare eyes; therefore, such FPs were referred to as LFPs (Zhao et al., 2016; Basavaraj et al., 2017a; Wang et al., 2017; Chen et al., 2015). Till date, numerous methods (chemical & optical) have been established to visualize LFPs. However, the recognition was restricted only to level 1 and level 2 ridge details due to the poor image qualities. Further, the level 1 and 2 features were easily forged by the use of artificial skin imprints. However, the analysis of level 3 features required some efficient nano powders with uniform particle size and morphology (Darshan et al., 2016a; Saif et al., 2013; Champod et al., 2004). The various phosphor nanomaterials used for visualize LFPs by various authors were listed in Table 1. By focused investigation of fingerprints, exhibits permanent, immutable and unique pores which were scattered on the ridges. For individual recognition, 20–40 pores were quite sufficient to establish the pore investigation (Labati et al., 2017). When a finger touches various surfaces, nonvolatile sweat constituents from the fingertip becomes immobilized on the surfaces, due to its highly networked structure. This confines the free migration of the constituents. Consequently, dot description of the pores rather than complete ridge patterns corresponds to fingertip ridges deposited on the surface. Unfortunately, sweat pores were the most neglected part due to non-availability of rapid, reliable and affordable FP visualization methods (Labati et

al., 2017). Hence, there was an urgent need to find a simple and efficient route for visualize LFPs with superior sensitivity, little background hindrance, extraordinary efficiency and lower toxicity, which was the essential requirement for forensic investigators (Darshan et al., 2016b; Rakesh et al., 2011; Dhanalakshmi et al., 2017).

The powder dusting approach became notably easy and flexible method for the LFPs visualization with superior visibility and detailed information. The visualization of LFPs via powder dusting technique includes the relevance of exceptional powder particles which shows higher affinity to moisture and adhering homes to the chemical compositions within the LFPs residue on numerous surfaces (Darshan et al., 2016c; Li et al., 2012). The form, size and surface vicinity of powder particles play a primary position for reinforcing LFPs. Labeling powders utilized for visualization of LFPs can categorized into three kinds; light, dark and phosphorescence powders. Sometimes, FPs visualized by using light and darkish powders was faint and exhibits low sensitivity on selected dark / light surfaces. However, combination of powders to gain effectiveness on each light and darkish surface also suffers for extremely faint impressions. In contrast, phosphorescence nanopowders were highly sensitive abounding with appropriate gentle property to visualize LFPs on porous and non-porous surfaces due to their exceptional physical and chemical properties together with massive surface region and high phosphorescence depth. Consequently, fluorescent / phosphorescence nanomaterials were the new agents for visualization of LFPs with high clarity on porous and non-porous surfaces (Darshan et al., 2016d).

Recently, rare earth doped nanophosphors were attracting considerable attention owing to their superior brightness, high efficiency, and long life time, as a result they were useful in plasma display panels (PDP), field emission displays (FEDs) and white light-emitting diodes

(WLEDs) (Filho et al., 2015; Chen et al., 2012; Lin et al., 2011; Zhang et al., 2015; Vijayakumar et al., 2015; Xia et al., 2013a; Xia et al., 2013b; Shi et al., 2014; Guogang et al., 2014). In recent times, oxyfluoride phosphors for WLED's have expanded much attention due to their improved properties such as thermal and chemical stability when compared to other hosts such as oxides, sulphides, molybdate, tungstate etc. (Dai et al., 2016; Chena et al., 2016; Fang et al., 2016; Chen et al., 2016; Xia et al., 2012c; Xia et al., 2014c; Kim et al., 2016).

Normally, phosphors with spherical morphology, narrow size distribution and free from agglomeration was highly essential because they exhibit low scattering of light and higher packing densities. Consequently, a superior method was required to develop above kind of phosphor materials for solid state lighting and forensic applications (Venkataravanappa et al., 2017; Venkatachalaiah et al., 2017, Basavaraj et al., 2017b). Rare earth (Sm^{3+}) ions were found to be essential activator for generating strong amber light emission. Sm^{3+} doped in stable luminescent host was more concern presently due to bright emission in orange or red regions (Xu et al., 2013; Wang et al., 2015; Luitel et al., 2012).

The rare earth doped LaOF materials were synthesized by various wet chemical routes including sol-gel, combustion, co-precipitation, etc. (Rakov et al., 2015; Bayarta et al., 2016; Li et al., 2015). From the numerous synthesis techniques stated above, ultrasound sonochemical synthesis method was advantageous over other routes due to fast production, relatively low temperature, low cost, and the easy way to accomplish high purity and single phase nanopowders. Sonochemistry comprises cavitation via energetic sound waves followed by formation of froths and bubbles in liquid which benefits for active nucleation and the evolution of nano/micro/superstructures (Suresh et al., 2017; Venkatachalaiah et al., 2017; Som et al., 2016a).

In the present work, Sm^{3+} doped LaOF NPs were prepared by ultrasound assisted sonochemical synthesis route using different surfactants such as Polyethylene glycol (PEG), Cetrimonium bromide (CTAB), Sodium dodecyl sulfate (SDS) and starch. The products were characterized by powdered X-ray diffraction (PXRD), scanning electron microscopy (SEM), transmission electron microscopy (TEM), diffuse reflectance spectra (DRS) and photoluminescence (PL). The optimized NPs were utilized to visualize the LFPs on non-porous surfaces. The photometric properties viz., Commission International de l 'Eclairage (CIE), correlated color temperature (CCT) and color purity were also evaluated and discussed in detail.

2. Experimental

2.1 Material and methods

Pure and Sm^{3+} (1-11 mol %) doped LaOF NPs were prepared via ultrasound assisted sonochemical method. The precursors used to prepare LaOF: Sm^{3+} NPs were of analytical grade with high purity and were purchased from Sigma Aldrich. The stoichiometric amount of Lanthanum nitrate [La $(NO_3)_3$ $4H_2O$ (99.9 %)], Ammonium fluoride [NH_4F (99.9 %)] and Samarium nitrate [Sm $(NO_3)_3$ (99.9 %)] were used in molar ratio of 1:2:1 and PEG, CTAB, SDS and Starch were used as surfactants. The detailed list of chemicals and surfactants used in the present study was given in Table 2. Initially, the precursor solutions were prepared by dissolution of La $(NO_3)_3$ and NH_4F in 50 ml of distilled water. Further, the required quantity of dopant ions and surfactants were added to the reaction mixture. The resulting final solution was subjected to ultrasound treatment (frequency of ~ 20 kHz, power of ~ 300 W and sonication time of ~ 1 - 6 h at a fixed temperature of 80 °C). The precipitate obtained at the end of the reaction was filtered using distilled water and alcohol. The powder was dried at 80 °C for 3 h in a hot air oven and

further heat treated at ~ 700 ^{o}C for 3 h. Fig.1. shows the schematic diagram of the ultrasonic synthesis of incorporated LaOF: Sm^{3+} NPs.

3. Characterization

The Shimadzu 7000 instrument was utilized to analyze the phase purity and crystallinity of the samples. Morphology was studied using Hitachi TM-3000 scanning electron microscope (SEM). Perkin Elmer (Lambda-35) spectrometer was used to record the diffused reflectance (DR) of the powder. PL spectra were recorded using Jobin Yvon Spectroflourimeter Fluorolog-3 attached with xenon lamp (450 W) as a source of excitation. The Hitachi H-8100, Transmission electron microscopy (TEM) was utilized for crystallite size analysis and for confirmation of chemical composition.

3.1 Visualization of LFPs and lip prints

LFPs were collected from the thoroughly washed and clean hands of healthy gently wiped across the forehead and pressed on the surfaces of different non-porous substrates surfaces. High PL intensity emitted composition was LaOF: Sm^{3+} (5 mol %) NPs were used for LFPs visualization. Carefully these compounds were stained on the surfaces of the substrates with a light brushing action and gently removed the excess powder until a fingerprint image was developed (Bandey, 2004). Stained fingerprints were photographed by a Nikon D3100/ AF-S Nikkor 50 mm f/1.8G ED lens digital camera under normal light. The schematic representation for the visualization of LFPs was shown in Fig.2.

In order to analyze the details of the lips print of the individuals, lips of healthy donor was washed thoroughly with water and cleaned with the cotton ball dipped in lipstick remover.

Clean and washed glass substrate on which lips impressions were taken. In the beginning, the glass slab was gently pressed starting from center and moving laterally in a single motion. After the proper lip impression on the glass slab, LaOF: Sm^{3+} (5 mol %) labeling agent was gently stained on the latent lip print with feather brush, thereafter the stained lip print was photographed with the camera under normal light.

4. Results and Discussion

In the present studies, undoubtedly visualized all the three levels of LFPs, i.e., level I (core), level II (bifurcation, bridge, ridge ending, crossover, island, enclosure, scar, eye and delta) and level III (sweat pores) by using LaOF: Sm^{3+} (5 mol %) labeling agent and observed under normal light (Fig.3). Further, the minutiae ridge details as well as powder distribution on the ridges were studied by SEM studies (Fig.3). The obtained images clearly demonstrated that the powder particles were uniformly distributed on the ridges due to identical sized particles with superior adhesive ability.

Fig.4 depicts the enhanced LFPs on various non-porous surfaces such as remote, wooden bar, steel plate, metal shield, metal scale and marble. From the figure, it was observed that the FPs was clearly visible with level I and level II ridge details. Whereas, the sweat pores were clearly visible on the surface of wooden sheet and stainless steel plate (Fig.4 (b & c)). Further, the LFPs were also tested on the other surfaces namely; glass slab, cell phone, glass bottle, calculator, compact disk, aluminium foil and etc. and obtain the requisite information for forensic investigators (Fig.5 (a-f)). The post processed FP images of level I, level II and level III minutiae ridges on aluminum foil were studied and depicted in Fig.5 (g - j). LFPs images of different donors were also investigated as shown in Fig.6. FPs of four different healthy donors were collected on the surface of aluminum foil and dusted with the optimized NPs. It was

observed from the figures that all the FPs was unique and easily identifies the ridge details. As it was observed from the Fig.6 (a & d), the FP images of the first and fourth donors resemble central and pocket whorl type. However, the second and third donors resemble plain and ulnar arch (Fig.6 (b & c)). In order to check the efficiency of the prepared NPs, the overlapped fingerprints were studied on aluminum foil surface (Fig.7). From the figure it was evident that, all the three levels minutia ridge patterns were visible. This indicates that the present powder can also be used effectively as a labeling agent for visualize complex FP patterns.

Cheiloscopy also known as lip print technique was one of the forensic investigation for identifying the individual humans based on lip traces. Characteristics of lip pattern of any individual were due to sulci laborium glands of labial mucosa on wrinkles and grooves. Observed wrinkles and grooves were named as sulci laborium rubrorum (Kaul et al., 2015). The continual moisturizing by the tongue due to occasional sebaceous glands present on the lips leaves behind the latent lip prints on various material surfaces such as glasses, cigarettes, straws, food items etc. Normally, the lip on these surfaces were not visible, some extra effort has to be paid to make the lip prints visible. In the present work, the powder dusting technique has been utilized to visualize lip print on glass surface. Fig.8 shows the lip print dusted with the LaOF: Sm^{3+} (5 mol %) NPs. The detailed classifications of the lip prints as indicated by Tsuchihashi were studied. All the five types of grooves (Type I to V) were clearly observed due to the smaller and uniform sized NPs.

Fig.9 shows the PXRD patterns of LaOF NPs prepared via conventional stirring and ultrasonication method. It was observed from the figure that a tetragonal phase along with some byproducts was formed by the conventional stirring method. However, in the case of ultrasonication, the highly crystalline and impurity - free phase was observed and it well matches

with the JCPDS, NO: 89-5168 with space group P4/nmm (No.129) (Luo et al., 2012). The effects of different surfactants namely PEG, CTAB, SDS and starch on Sm^{3+} doped LaOF NPs were studied, as shown in Fig.10. All the PXRD profiles were well matched with standard JCPDS, NO: 89-5168 without any impurities. The average crystallite size (D) was estimated using Scherrer's relation (Suresh et al., 2017).

$$D = 0.9\lambda / \beta \cos\theta \quad \text{---------- (1)}$$

where, λ : wavelength of the X-rays (1.541 Å), β : full- width at half maximum (FWHM) on 2θ scale and θ : Bragg's angle. Further, the value of D and strain present within the prepared sample was evaluated using W - H approach (Zhu et al., 2005).

$$\frac{\beta \cos\theta}{\lambda} = \frac{0.9}{d} = \frac{\varepsilon \sin\theta}{\lambda} \quad \text{---------- (2)}$$

where β *:* FWHM in radians, ε : the strain, D : the crystallite size and θ : Bragg's diffraction angle. The plot of βcosθ/λ versus sinθ/λ signifies W-H plots, as shown in Fig.10 (d). The slope and intercept of this linearly fit plot provides micro-strain within the sample and crystallite size. The estimated values were tabulated in Table 3. The higher strain was found for the Sm^{3+} doped samples because the addition of Sm^{3+} ions leads to the host lattice distortion.

To evaluate the structural parameters, the PXRD profiles were refined for various lattice parameters, Pseudo-Voigt profile function (u, v and w), isothermal temperature factors (B_{iso}), by considering backgrounds scale factor and atomic co-ordinates (Dhananjaya et al., 2016). The recorded, calculated and the difference PXRD patterns of pure and Sm^{3+} doped LaOF were shown in Fig.11 (a, c-h). The experimental and calculated data of PXRD profiles showed nearly to zero in the intensity scale as illustrated by a line (Y_{obs}–Y_{calc}). The packing diagram of LaOF: Sm^{3+} (5 mol %) was shown in Fig.11 (b). The structural parameters refined by Rietveld analysis

for LaOF: Sm^{3+} (1- 11 mol %) NPs were summarized in Table 4. The unit cell parameters decrease after the substitution of Sm^{3+} ion (R_d = 1.066 Å) for 8 coordinated La^{3+} (R_s = 1.160 Å) site in the LaOF lattice. The acceptable percentage difference (D_r) between dopant Sm^{3+} and La^{3+} should not exceed 30 %. The value of D_r between the doped ions (Sm^{3+}) and substituted ions (La^{3+}) in LaOF: Sm^{3+} NPs was estimated based on the formula (Darshan et al., 2016a):

$$D_r = \frac{Rm(CN) - Rd(CN)}{Rm(CN)} \quad \text{---------- (3)}$$

where CN : Co-ordination number, R_m (CN) : radius of host cations and R_d (CN) : radius of dopant ion and it was found to be 25 %. Thus, it clearly indicates that the ionic radius of Sm^{3+} was close to that of La^{3+}. Hence, it was assumed that the La^{3+} site was replaced by Sm^{3+} ions in the lattice.

The diffuse reflectance (DR) spectra of LaOF: Sm^{3+} (1- 11 mol %) NPs recorded at RT in the range of 200-1100 nm was shown in Fig. 12(a). The spectra exhibited dominant peaks at 357, 405,446, 478, 529, 586, 939 and 1070 nm due to the transitions of the 4f electrons of Sm^{3+} from the ground-state to $^6H_{5/2} \rightarrow {}^4H_{7/2}$, $^6H_{5/2} \rightarrow {}^4F_{7/2,}$ $^6H_{5/2} \rightarrow {}^4G_{9/2}$, $^6H_{5/2} \rightarrow {}^4I_{11/2,}$ $^6H_{5/2} \rightarrow {}^4F_{3/2}$, $^6H_{5/2} \rightarrow {}^4G_{5/2}$, $^6H_{5/2} \rightarrow {}^4F_{11/2}$ and $^6H_{5/2} \rightarrow {}^4F_{9/2}$ respectively (Shang et al., 2012; Xie et al., 2012). Further, the energy gap (E_g) of the prepared NPs was estimated by applying the Kubelka–Munk (K-M) theory to DR spectra. The plots of $[F(R_\infty)h\nu]^{1/2}$ versus photon energy ($h\nu$) were shown in Fig. 12 (b). The Kubelka–Munk function F (R_∞) and photon energy ($h\nu$) were estimated using the relations (Amith et al., 2017; Xiao et al., 2010):

$$F(R_\infty) = \frac{(1-R_\infty)^2}{2R_\infty} \quad \text{---------- (4)}$$

$$h\nu = \frac{1240}{\lambda} \text{ ---------- (5)}$$

where R_∞ and λ were the reflection coefficient and absorption wavelength, respectively. Further, refractive indexes (R.I) of the samples were estimated using the relation;

$$\frac{n^2_r - 1}{n^2_r + 1} = 1 - \sqrt{\frac{E_g}{20}} \text{ ---------- (6)}$$

The estimated E_g and R.I values were tabulated in Table 5. From the table, it was clear that E_g and R.I values increases with increase of dopant concentration. The variation in E_g and refractive index was associated with quantum confinement effect in nano-size particles i.e. the squeezing of electron hole pair below the dimensions approaching exciton Bohr radius and with the intermediate localized states in the band gap due to structural defects (Shahi et al., 2009).

Fig.13 shows the SEM micrographs of LaOF: Sm^{3+} (5 mol %) NPs prepared with four different surfactants namely PEG, CTAB, SDS and starch under 3 h sonication time. The cubic and hexagonal discs were observed for PEG used sample (Fig.13 (a)). The agglomerated flake - like structures with indefinite shape were identified in CTAB and starch assisted samples (Fig.13 (b & d)). However, the SDS assisted products exhibited agglomerated particles with pores and voids (Fig.13 (c)). From these results, it was evident that the PEG surfactant one could able to obtain various shapes and sized particles. Fig.14 shows the mechanism for the formation of spherical shaped nanostructures in the presence of PEG.

Fig.15 (A) shows the SEM micrographs of LaOF: Sm^{3+} (5 mol %) NPs synthesized with different sonication time (1-6 h) while PEG surfactant was fixed to 30 ml. Initially, when the sonication time was 1-2 h, that elongated particles attached each other (Fig.15 (A) (a & b)). Further, when the sonication time was increased to 3-5 h, these particles were separated and to form a network - like structure (Fig.15 (A) (c-e)). Further, when the sonication time was

extended to 6 h, plate - like structures were noticed (Fig.15 (A), (f)). This confirms that the sonication time influences considerably in the modification of morphology of the product.

The effect of PEG concentration (5 – 30 ml) on the product morphology was studied, as shown in Fig. 15 (B). When PEG surfactant volume was ~ 5 ml, prisms like microstructures were observed (Fig.15 (B) (a)). When PEG volume was increased from ~ 5 to 10 ml, almost spherical shaped particles along with mesh like morphology were noticed (Fig.15 (B) (b)). However, when the PEG volume was ~ 15 ml, the hexagonal prism-like structures were obtained Fig.15 (B) (c)). The smooth edged dice - like network particles were formed when the PEG volume was ~ 20 ml (Fig.15 (B) (d)). When the PEG volume was increased to ~ 25 ml, the elongated dumbbell shaped structures were obtained (Fig.15 (B) (e)). Finally, a spindle shaped network was formed when the PEG volume was increased to 30 ml (Fig.15 (B) (f)). The results clearly indicate that the surfactant volume plays a vital role in product morphology engineering. The effects of pH and sonication power on the product morphology were also studied, as shown in Fig.16 (A) & (B). From the figure, it was clear that the nest - like structure was commonly observed for all pH and sonication power.

Fig.17 shows the TEM, HRTEM images, SAED patterns and EDX analysis of LaOF: Sm^{3+} (5 mol %) NPs prepared with PEG, CTAB and SDS surfactants under 3 h sonication time. The particles were obtained as hexagonal and flake like structures, which was in good agreement with the SEM results. Further, the particles sizes for all the surfactants lie in the range of ~ 20 - 35 nm. Further, the SAED pattern the product exhibits highly crystalline nature. The interplanar spacing values (d) were estimated to be ~ 0.32, 0.30 and 0.28 nm. In Fig. 17 (j & k), the EDAX spectrum shows the strong La line at ~ 4.954 keV, O line at ~ 0.827 keV, F line at ~ 0.954 keV , and small traces of Sm line showing that there was no trace of other by products. In other words,

no elements other than LaOF: Sm^{3+} and oxygen were detected which confirm the purity of the prepared NPs synthesized in the present work.

The PL excitation spectrum of doped LaOF: Sm^{3+} (5 mol %) NPs monitored at 607 nm emission wavelength were shown in Fig.18 (a). The spectrum exhibits peaks at ~ 343, 361, 377, 406, 414, 449, 467 and 480 nm corresponding to $^6H_{5/2} \rightarrow {}^4K_{17/2}+{}^4L_{17/2}$, $^6H_{5/2} \rightarrow {}^4D_{15/2}+{}^6P_{15/2}$, $^6H_{5/2} \rightarrow {}^4L_{17/2}$, $6H5_{/2} \rightarrow {}^4K_{11/2}$, $^6H_{5/2} \rightarrow {}^6P_{5/2}+{}^6M_{19/2}$, $^6H_{5/2} \rightarrow {}^4G_{9/2}+{}^4I_{15/2}$, $^6H_{5/2} \rightarrow {}^6P_{5/2}+{}^6M_{19/2}$, $^6H_{5/2} \rightarrow {}^4G_{9/2}+{}^4I_{15/2}$, $^6H_{5/2} \rightarrow {}^4F_{5/2}+{}^4I_{13/2}$ and $^6H_{5/2} \rightarrow {}^4I_{11/2}+{}^4M_{15/2}$ transitions of Sm^{3+} ions respectively (Kang et al., 2011). Fig. 18 (b) shows the PL emission spectra of LaOF: Sm^{3+} (1 - 11 mol %) NPs excited at 406 nm. The spectra exhibit strong emission peaks at ~ 566, 607, 653 and 708 nm attributed to $^4G_{5/2} \rightarrow {}^6H_{5/2}$, $^4G_{5/2} \rightarrow {}^4H_{7/2}$, $^4G_{5/2} \rightarrow {}^6H_{9/2}$ and $^4G_{5/2} \rightarrow {}^6H_{11/2}$ intra - 4f orbital transitions of Sm^{3+} ions respectively (Zou et al., 2017; Atuchin et al., 2015). Among these transitions, the peaks at ~ 566 nm ($^4G_{5/2} \rightarrow {}^6H_{5/2}$), ~ 607 nm ($^4G_{5/2} \rightarrow {}^6H_{7/2}$) and ~ 653 nm ($^4G_{5/2} \rightarrow {}^6H_{9/2}$) were magnetic-dipole (MD), partly forced electric-dipole (ED) transition, and purily ED transition, respectively (Kodaira et al., 2007a). Notably, the peak at ~ 607 nm ($^4G_{5/2} \rightarrow {}^6H_{7/2}$ transion) has the strongest intensity and it was applied to orange-red emitting display materials. The inensity ratio (Asymmetry ratio (A_{21})) of ED and MD trasitions can be used to understand the distortion degree from the inversion symmetry of the Sm^{3+} local environment in the host (Shi et al., 2016). In the present case, the value of A_{21} increases with increase of Sm^{3+} concentration up to 3 mol % and then decreases. This variation of A_{21} values can influence the luminescent property of a sample. It was evidence that the PL intensity increased up to 5 mol % of Sm^{3+} and after this, it diminished. The variation of PL intensity and A_{21} value with Sm^{3+} ion concentration was shown in Fig. 18 (c). The PL emission intensity

decrease was due to well-known self-concentration quenching phenomenon attributed to energy transfer among the Sm^{3+} ions in the LaOF host (Tiana et al., 2012).

To know more about concentration quenching, it was significant to elucidate the interaction mechanism, which usually happens due to exchange interaction, re-absorption or a multiple – multiple interaction. Therefore, it was essential to calculate the critical distance (R_c) between the two Sm^{3+} ions in LaOF host by using following relation (Li et al., 2009);

$$R_c = 2\left(3V/4\pi NX_c\right)^{1/3} \text{ ---------- (7)}$$

where V; unit cell volume, X_c; critical concentration of Sm^{3+} ions and N; number of crystallographic sites per unit cell. The estimated value of R_c was found to be ~ 21 Å. According to Van Uitert's, the exchange interaction was possible only the if value of R_c was below 5 Å. In the present work, the R_c value was found to be greater than 5 Å which evidenced that the energy transfer process should be attributed to multipole–multipole interaction.

According to Van Uitert model, the type electric multipolar interaction was estimated using the following relation (Shi et al., 2015);

$$\frac{I}{\chi} = K\left[1+\beta(\chi)^{\frac{Q}{3}}\right]^{-1} \text{ ---------- (8)}$$

where χ ; Sm^{3+} ions concentration, Q ; a constant of electric multipolar interaction having values 3, 6, 8 and 10 indicating exchange interactions, dipole–dipole (*d–d*), dipole–quadrupole (*d–q*) and quadrupole–quadrupole (*q–q*) interactions respectively and K & β ; constants for the given host crystal (Nair et al., 2016). Logarithmic plot of (I/x) v/s (x) exhibits a linear graph with a slope ~ - 1.70 and intercept = 5.92 was shown in Fig.18 (d). The value of Q was calculated to be

~ 5.1 that was close to 6, and it indicates that the *d–d* interaction was responsible for concentration quenching in the present samples.

The Judd-Ofelt (J – O) intensity parameters (Ω_2 & Ω_4) and different radiative properties such as radiative transition probability (A_T), radiative (τ_{rad}) lifetime, branching ratio (β_R) and asymmetric ratio (A_{21}) were calculated for detailed investigation of site symmetry as well as luminescence dynamics of Sm^{3+} ions in LaOF matrix (Judd, 1962; Ofelt, 1962). Although J – O analysis was a influential tool, which efficiently defines the spectral behavior in a specific coordination location of rare earth ion incorporated single and polycrystalline materials, glasses and solutions. Detailed physical interpretation J-O parameters were given by Jorgensen and Reisfeld (Jorgensen et al., 1983). These parameters were estimated from the PL emission spectra considering magnetic dipole allowed transition ($^5G_{5/2} \rightarrow {}^6H_{7/2}$) as the reference, since it was unchanged by the neighboring crystal field environment. The rates of parity forbidden dipole transitions among various electronic states of the rare earths, local structural environment surrounding them and covalent bonds associated ligands of them can easily evaluated by this J-O analysis (Som et al., 2015b). The relation between radiative emission rates and the integrated emission intensities were calculated by the relations (Feng et al., 2013);

$$\frac{A_{0-2,4}}{A_{0-1}} = \frac{I_{0-2,4}}{I_{0-1}} = \frac{h\upsilon_{0-1}}{h\upsilon_{0-2,4}} \text{ ---------- (9)}$$

where $I_{0\text{-}J}$ and $h\nu_{0-J}$: integrated emission intensity and energies corresponding to transition $^4G_{5/2} \rightarrow {}^6H_J$ (J=5/2, 7/2, 9/2) respectively.

The radiative emission rates ($A_{0\text{-}J}$) of electric dipole related with J-O parameters was expressed as (Kodaira et al., 2003b);

$$A_{(0-J)} = \frac{64\pi^4 \nu_J{}^3}{3h(2J+1)} \frac{n\left(n^2+2\right)^2}{9} \sum_{J=2,4} \Omega_J \left| \left\langle {}^4G_{5/2} \left\| U^{(J)} \right\| {}^6H_J \right\rangle \right|^2 \text{ ---------- (10)}$$

where, e : the electronic charge, ν_J : the wave number of the corresponding transition, h : the Planck's constant, n : the RI of the prepared sample. $\left|\left\langle {}^4G_{5/2}\left\|U^{(J)}\right\|^6 H_J\right\rangle\right|^2$: the squared reduced matrix elements of Sm^{3+} ions independent of the chemical environment [23]. Thus by using Eqs. (9) and (10), the values of Ω_2 and Ω_4 were estimated and tabulated in Table 5. The intensity parameters Ω_2 and Ω_4 were due to short range and long-range effect respectively. The variation of Ω_2 with different Sm^{3+} concentration indicates that Ω_2 was more sensitive to the ligand environment. This means that Ω_2 value was ascribed to the covalency and structural changes in the locality of the Sm^{3+} ions exhibiting short range effect whereas the parameter Ω_4 was dependent on the viscosity and dielectric constant of the host influences the long range effect. In the present case, the Ω_2 value was increased with the Sm^{3+} concentration increase up to 5 mol %, and that shows stronger covalence of Sm-O bonding and lower symmetry around the Sm^{3+} ions.

The radiative transition probability (A_T) was determined by using the relation;

$$A_T(\psi_J) = \sum_{J'} A_{J-J'} \text{ ---------- (11)}$$

The radiative lifetime (τ_{rad}) of an excited state can be expressed as

$$\tau_{rad}(\psi_J) = \frac{1}{A_T(\psi_J)} \text{ ---------- (12)}$$

The branching ratio $\beta(\psi_J)$ corresponding to the emission from an excited level to its lower level was given by (Som et al., 2015b);

$$\beta(\psi_J) = \frac{A(\psi_J, \psi'_{J'})}{A_T(\psi_J)} \text{ ---------- (13)}$$

The radiative properties, namely radiative transition probabilities (A_T), radiative lifetimes (τ_{rad}) and branching ratios (β_R), for the excited states of Sm^{3+} ion were estimated using J–O parameters

and tabulated in Table 5. Since the branching ratio (β) of the optimized phosphor was found to be higher than 0.50, it was potentially useful in solid state lightning applications.

The CIE chromaticity diagram (Smith et al., 1931) of LaOF: Sm^{3+} (1-11 mol %) NPs was presented in Fig.18 (e). It was evident that the CIE chromaticity coordinates were located in the orange-red region. To identify applicability of this orange-red emission, the CCT was estimated from CIE coordinates. Fig.18 (f) shows the CCT diagram of LaOF: Sm^{3+} (1-11 mol %) NPs. The CCT was a specification of the color appearance of the light emitted by a light source, relating its color to the color of light from a reference source when heated to particular temperature. The correlated color temperature (CCT) was one of the essential parameter to know the color appearance of the light emitted by a light source with respect to a reference light source when heated up to a specific temperature, in Kelvin (K). CCT was estimated by transforming the (x, y) co-ordinates of the light source to (U_0, V_0) by using the eqn. (6) and (7), and by determining the temperature of the closest point of the Planckian locus to the light source on the (U_0, V_0) uniform chromaticity diagram**;**

$$U_0 = \frac{4x}{-2x+12y+3} \text{ ---------- (14)}$$

$$V_0 = \frac{9y}{-2x+12y+3} \text{ ---------- (15)}$$

Also, the quality of white light in terms of color correlated temperature (CCT) was given by McCamy empirical formula $CCT = -437n^3 + 3601n^2 - 6861n + 5514.31$(theoretical) where $n = (x - x_c)/(y - y_c)$; the inverse slope line and chromaticity epicenter was at x_c= 0.3320 and y_c= 0.1858. Generally, CCT value was greater than 5000 K indicates the cold white light used for commercial lighting purpose (Meetei et al., 2014). The estimated CIE co-ordinates (x, y), (U_0,

V_0) and CCT values of LaOF: Sm^{3+} (1-11 mol %) NPs were tabulated in Table 6. Thus, the present phosphor can be useful for artificial production of white light in illumination devices.

The Quantum efficiency (Q_E) of the optimized LaOF: Sm^{3+} (5 mol %) NPs was estimated using the relation reported elsewhere (Mello et al., 1997). The estimated value of Q_E was found to be ~ 88.14 %. Colour purity (CP) of the prepared sample was also checked using following relation (Chhajed et al., 2005);

$$color\ \ purity = \frac{\sqrt{(x_s - x_i)^2 + (y_s - y_i)^2}}{\sqrt{(x_d - x_i)^2 + (y_d - y_i)^2}} \times 100\% \text{ ---------- (16)}$$

where (x_s, y_s) :the coordinates of a sample point, (x_d, y_d) : the coordinates of the dominant wavelength and (x_i, y_i) : illuminant point coordinates. The CP of the prepared samples were estimated and tabulated in Table 5. The CP of optimized sample was found to be ~ 82.3 %.

The luminescence decay of prepared LaOF: Sm^{3+} (1, 5, & 11 mol %) NPs was realized by fitted with following bi-exponential decay equation;

$$I(t) = I_1 e^{-\frac{1}{\tau_1}} + I_2 e^{-\frac{1}{\tau_2}} \text{ ---------- (17)}$$

where I_1 and I_2: intensities at different times and their corresponding lifetimes τ_1 and τ_2.

The average lifetime in case of a bi-exponential decay can be calculated using the equation;

$$\tau_{avg} = \frac{I_1\tau_1^2 + I_2\tau_2^2}{I_1\tau_1 + I_2\tau_2} \text{ ---------- (18)}$$

The multi exponential decay may be explained as: (i) Difference in the nonradiative probability of decays for lanthanide ions at or near the surface and lanthanide ions in the core of the particles. (ii) Inhomogeneous distribution of the doping ions in the host material leading to the variation in the local concentration. (iii) The transfer of excitation energy from donor to lanthanide activators (Som et al., 2014c). In the present work, the variation in the luminescence

decay of prepared LaOF: Sm^{3+} (1, 5, & 11 mol %) NPs (Fig.19) due to structural defects and the presence of several Sm^{3+} sites in the matrix may impact the emission. This indicates that the prepared phosphor might be excellent materials for the WLED applications.

5. Conclusions

In summary, preparation of series of LaOF: Sm^{3+} (1-11 mol %) NPs using non-toxic, eco-friendly ultrasound assisted sonochemical method using four different surfactants was reported. Particles morphology can be greatly engineered by varying experimental parameters, namely sonication time, volume of the surfactant, pH value, temperature of sonication bath and sonication power. PXRD and TEM / HRTEM analysis revealed the crystallite size ~ 20 nm and interplanar spacing ~ 0.32 nm. Prepared NPs exhibit excellent photometric characteristics and they can be used to fill amber gap in LEDs under near-UV excitation. Optimized NPs have been effectively used as labeling agent to visualize LFPs on various non-porous surfaces under normal light. LFPS were visualized with high sensitivity, low background hindrance, high efficiency and low toxicity due to the quality of prepared nanophosphor materials adherence efficiency. These results clearly indicate the utility of LaOF: Sm^{3+} (5 mol %) NPs in visualization of LFPs, lips print as well as useful component in solid state lighting applications.

Acknowledgement

The author Dr. H Nagabhushana thanks to VGST (No: CWASEE/K-FWAST L1, GRD No.489) Karnataka for the sanction of this Project.

References

Amith Yadav, H.J., Eraiah, B., Nagabhushana, H., Darshan, G.P., Daruka Prasad, B., Sharma, S. C., Premkumar, H.B., Anantharaju, K.S., Vijayakumar, G.R., 2017. Facile ultrasound route to prepare micro/nano superstructures for multifunctional applications, ACS Sustain. Chem. Eng. 5, 2061−2074.

Atuchin, V. V., Aleksandrovsky, A. S., Chimitova, O. D., Cheng-Peng Diao, Gavrilova, T. A., Kesler, V. G., Molokeev, M. S., Krylov, A. S., Bazarov, B. G., Bazarova, J. G., Zheshuai Lin, 2015. Electronic structure of β-RbSm $(MoO_4)_2$ and chemical bonding in molybdates, Dalton. Trans. 44, 1805-1815.

Bandey, H. L., 2004. Fingerprint development and imaging newsletter: the powders process, study 1. Sandridge, UK: Police Scientific Development Branch, Home Office, Report No.54/04.

Basavaraj, R. B., Nagabhushana, H., Darshan, G.P., Daruka Prasad, B., Sharma, S.C., Venkatachalaiah, K.N., 2017. Ultrasound assisted rare earth doped Wollastonite nanopowders: Labeling agent for imaging eccrine latent fingerprints and cheiloscopy applications, J. Ind. Eng. Chem. 51, 90-105.

Basavaraj, R.B., Nagabhushana, H., Daruka Prasad, B., Vijayakumar, G.R., 2017. Zinc silicates with tunable morphology by surfactant assiasted sonochemical route suitable for NUV excitable white light emitting diodes, Ultrason. Sonochem. 34, 700–712.

Bayarta, A., Katelnikovasb, A., Blacha, J-F., Rousseaua, J., Saitzeka, S., 2016. Synthesis, structural and luminescence properties of $(La_{1-x}Ln_x)_2$ Ti_2O_7 (Ln=lanthanides) solid solutions, J. Alloy Compd. 683, 634–646.

Cao Y., Liu N., Yang P., Shi R., Ma Q., Zhang A., 2014, Aqueous synthesis of MPA-capped CdTe nanocrystals emitted in near infrared with high quantum yield, J Nanosci Nanotechnol., 14, 5238-5243.

Chen, H., Chang, K., Men, X., Sun, K., Fang, X., Ma, C., Zhao, Y., Yin, S., Qin, W., Wu, C. F., 2015. Covalent patterning and rapid visualization of latent fingerprints with photo-cross-linkable semiconductor polymer dots, ACS Appl. Mater. Inter. 7, 14477−14484.

Champod, C., Lennard, C., Margot, P., Stoilovic, M., 2004. Fingerprints and other ridge skin impressions. CRC Press.

Chen, L., Chu, C.I., Liu, R.S., 2012. Improvement of emission efficiency and color rendering of high-power LED by controlling size of phosphor particles and utilization of different phosphors, Microelectron. Reliab. 52, 900-904.

Chena, Y., Zhoub, B., Suna,Q., Wanga,Y., Yana, B., 2016. Synthesis and luminescence properties of $Sr_3MgSi_2O_8$: Ce^{3+}, Tb^{3+} for application in near ultraviolet excitable white light-emitting-diode, Superlattices Microst. 100, 158–167.

Chen, J., Zhang, N., Guo, C., Pan, F., Zhou, X., Suo, H., Zhao, X., Goldys, E. M., 2016, Site-dependent luminescence and thermal stability of Eu^{2+} doped Fluorophosphate toward white LEDs for plant growth, ACS Appl. Mater. Inter. 8, 20856–20864.

Choi M J, Mcbean. K, Ng. P.H. R. McDonagh, A. M. Maynard, P. J., Lennard, C,, Roux C., 2008, An evaluation of nanostructured zinc oxide as a fluorescent powder for fingerprint detection, J. Mater. Sci., 43, 732-737.

Chhajed, S., Xi, Y., Li, Y.-L., Gessmann. Th., Schubert, E. F., 2005. Influence of junction temperature on chromaticity and color-rendering properties of trichromatic white-light sources based on light-emitting diodes, J. Appl. Phys. 97, 1-8.

Darshan, G.P., Premkumar, H.B., Nagabhushana, H., Sharma, S.C., Prashantha, S.C., Daruka Prasad, B., 2016. Effective fingerprint recognition technique using doped yttrium aluminate nano phosphor material, J. Colloid Interf. Sci. 464, 206-218.

Darshan, G.P., Premkumar, H.B., Nagabhushana, H., Sharma, S.C., Prashantha, S.C., Nagaswarupa, H.P., Daruka Prasad, B., 2016. Blue light emitting ceramic nano-pigments of Tm^{3+} doped $YAlO_3$: Applications in latent finger print, anti-counterfeiting and porcelain stoneware, Dyes Pigment. 131, 268-281.

Darshan, G.P., Premkumar, H.B., Nagabhushana, H., Sharma, S.C., Daruka Prasad, B., Prashantha, S.C., Basavaraj, R.B., 2016. Superstructures of doped yttrium aluminates for luminescent and advanced forensic investigations, J. Alloy Compd. 686. 577-587.

Darshan, G.P., Premkumar, H.B., Nagabhushana, H., Sharma, S.C., Daruka Prasad, B., Prashantha, S.C., 2017. Neodymium doped yttrium aluminate synthesis and optical properties–A blue light emitting nanophosphor and its use in advanced forensic analysis, Dyes Pigment. 134, 227-2335.

Dai, P., Cao, J., Zhang, X., Liu, Y., 2016. Bright and high-color-rendering white light-emitting diode using color-tunable oxychloride and oxyfluoride phosphors, J. Phys. Chem. C 120, 18713−18720.

Dhanalakshmi, M., Nagabhushana, H., Darshan, G.P., Basavaraj, R.B., Daruka Prasad, B., 2017. Sonochemically assisted hollow/solid $BaTiO_3$:Dy^{3+} microspheres and their applications in effective detection of latent fingerprints and lip prints, J. Sci.: Adv. Mat. Dev. 2, 22–33.

Dhananjaya, N., Shivakumara, C., Saraf, R., Nagabhushana, H., 2016. Red-emitting LaOF:Eu^{3+} phosphors: Synthesis, structure and their Judd–Ofelt analysis for LED applications, Mater. Res. Bull. 75, 100–109.

Donghyeon Kim, Sung-Chul Kim, Jong-Seong Bae, Sungyun Kim, Seung-Joo Kim, Jung-Chul Park, 2016. Eu^{2+}-Activated alkaline-Earth halophosphates, $M_5(PO_4)_3X:Eu^{2+}$ (M = Ca, Sr, Ba; X = F, Cl, Br) for NUV-LEDs: Site-selective crystal field effect, Inorg. Chem. 55 (17), 8359–8370.

Fang, M-H., Ni, C., Zhang, X., Tsai, Yi-Ti., Mahlik, S., Lazarowska, A., Grinberg, M., Sheu, H-S., J-F. , Cheng, B -M., Liu, R-S., 2016. Enhance color rendering index via full spectrum employing the important key of cyan phosphor, ACS Appl. Mater. Inter. 45, 30677–30682.

Feng, J., Zhang, H., 2013. Hybrid materials based on lanthanide organic complexes: a review, Chem. Soc. Rev. 42, 387-410.

Gao F., Caifeng L., Jiaxing H., Xiyeu L., Qin W., Jun Z., Cheng C., Qun L., Xiufeng S., Jincheng Z., Liru B., Xin L., 2011, CdTe-Montmorillonite nanocomposites: control synthesis, UV radiation dependent photoluminescence and enhanced latent fingeriprint detection, J. Phys. Chem. C., 115, 21574-21583.

Guogang Li, Chun Che Lin, Wei-Ting Chen, Maxim S. Molokeev, Victor V. Atuchin, Chang-Yang Chiang, Wuzong Zhou, Chin-Wei Wang, Wen-Hsien Li, Hwo -Shuenn Sheu, Ting-Shan Chan, Chonggeng Ma,Ru-Shi Liu, 2014. Photoluminescence tuning via cation substitution in Oxonitridosilicate phosphors: DFT calculations, different site occupations, and luminescence mechanisms, Chem. Mater. 26 (9), 2991–3001.

Jorgensen, C.K., Reisfeld, R., 1983. Judd-Ofelt parameters and chemical bonding, J. Less-Common Met. 93, 107-112.

Judd, B. R., 1962. Optical absorption intensities of rare-earth ions, Phys. Rev. 127, 750-761.

Kaul, R., Padmashree, S. M., Shilpa, P. S., Sultana, N., Bhat, S., 2015. Cheiloscopic patterns in Indian population and their efficacy in sex determination: A randomized cross-sectional study, J. Forens. Dental Sci.7, 101–106.

Kang, D., Yoo, H. S., Jung, S. H., Kim, H., Jeon, D. Y., 2011. Synthesis and Photoluminescence Properties of a Novel Red-Emitting $Na_2Y_2Ti_3O_{10}:Eu^{3+}$, Sm^{3+} Phosphor for White-Light-Emitting Diodes, J. Phys. Chem. C, 115, 24334–24340.

Kodaira, C.A., Stefani, R., Maia, A.S., Felinto, M.C.F.C., Brito H.F., 2007. Optical investigation of $Y_2O_3:Sm^{3+}$ nanophosphor prepared by combustion and Pechini methods, J. Lumin. 127, 616–622.

Kodaira, C. A., Brito, H. F., Malta, O. L., 2003. Luminescence and energy transfer of the europium (III) tungstate obtained via the Pechini method, J. Lumin.101, 11–21.

Labati, R. D., Genovese, A., Muñoz, E., Piuri, V., Scotti, F., 2017. A novel pore extraction method for heterogeneous fingerprint images using convolutional neural networks, Pattern Recog. Lett. https://doi.org/10.1016/j.patrec.2017.04.001.

Li, Y., Xu, L., Su, B., 2012. Aggregation induced emission for the recognition of latent fingerprints, Chem. Commun. 48, 4109-4111.

Li, R., Yu, G., Liang, Y., Zhang, N., Liu, Y., Gan, S., 2015, Morphology-controllable synthesis of LaOF:Ln^{3+} (Ln = Eu, Tb) crystals with multicolor luminescence properties, J. Colloid Interf. Sci. 460, 273–280.

Li, P., Wang, Z., Yang, Z., Guo, Q., Li, X., 2009. Emission features of $LiBaBO_3$:Sm^{3+} red phosphor for white LED, Mat. Lett. 63, 751–753.

Luitel, H. N., Watari, T., Chand, R., Torikai,T., Yada, M., 2012. Photoluminescence properties of a novel orange red emitting $Sr_4Al_{14}O_{25}$:Sm^{3+} phosphor and PL enhancement by Bi^{3+} co-doping, Opt. Mater. 34, 1375–1380.

Luo, Y., Xia, Z., Liao, L., 2012. Phase formation evolution and up conversion luminescence properties of LaOF: Yb^{3+}/Er^{3+} prepared via a two-step reaction, Ceram. Int. 38, 6907–6910.

Meetei, S. D., Singh, S. D., 2014. Hydrothermal synthesis and white light emission of cubic ZrO_2:Eu^{3+} nanocrystals, J. Alloy Compd. 587, 143.

Mello de, J.C., Wittmann, H.F., Friend, R.H., 1997. An improved experimental determination of external photoluminescence quantum efficiency, Adv. Mater. 9, 230-232.

Nair, G. B., Dhoble, S. J., 2016. Photoluminescence properties of Eu^{3+}/ Sm^{3+} activated $CaZr_4(PO_4)_6$ phosphors, J. Fluoresc. 26, 1865–1873.

Ofelt, G. S., 1962. Intensities of crystal spectra of rare-earth ions, J. Chem. Phys. 37, 511-520.

Paulo, C., Filho, de S., Gacoin, T., Boilot, J-P., Walton, R. I., Serra, O. A., 2015. Synthesis and luminescent properties of $REVO_4$–$REPO_4$ (RE = Y, Eu, Gd, Er, Tm, or Yb) hetero nanostructures: A promising class of phosphors for excitation from NIR to VUV, J. Phys. Chem. C 42, 24062–24074.

Pinglu Shi, Zhiguo Xia, Maxim, S., Molokeev, Victor, V,. Atuchin, 2014. Crystal chemistry and luminescence properties of red-emitting $CsGd_{1-x}Eu_x(MoO_4)_2$ solid-solution phosphors, Dalton Trans. 43, 9669-9676.

Rakesh, K., Garg, H., Kumari, R., Kaur, 2011. A new technique for visualization of latent fingerprints on various surfaces using powder from turmeric: A rhizomatous herbaceous plant (Curcuma longa), Egyp. J. Forensic Sci. 1, 53–57.

Rakov, N., Vieira, S. A., Guimarães, R. B., Maciel, G. S., 2015. Investigation of Eu^{3+} luminescence enhancement in LaOF powders co doped with Tb^{3+} and prepared by combustion synthesis, J. Alloy Compd. 618, 127-131.

Saif, M., 2013. Synthesis of down conversion, high luminescent nano-phosphor materials based on new developed Ln^{3+}:$Y_2Zr_2O_7/SiO_2$ for latent fingerprint application. J. Lumin. 135, 187–195.

Shang, M., Li, G., Kang, X., Yang, D., Geng, D., Peng, C., Cheng, Z., Liana, H., Lin, J., 2012. LaOF: Eu^{3+} nanocrystals: hydrothermal synthesis, white and color-tuning emission properties, Dalton Trans. 41, 5571-5580.

Shi, R., Xu, J., Liu, G., Zhang, X., Zhou, W., Pan, F., Huang, Y., Tao, Y., Liang, H., 2016. Spectroscopy and Luminescence Dynamics of Ce^{3+} and Sm^{3+} in $LiYSiO_4$, J. Phys. Chem. C 120, 4529–4537.

Shi, X., Liu, Y., Zhang, J., Zhang, K., Li, P., H. Zuo, Li, J., 2015. Effects of pH and Sm^{3+} doping on the structure, morphology and luminescence properties of $BiPO_4$:Sm^{3+} phosphors prepared by hydrothermal method, Ceram. Int. 41, 3162–3168.

Smith, T., Guild, J., 1931. The C.I.E. colorimetric standards and their use, Transac. Opt. Soc. 33, 75 – 134.

Som, S., Kumar, V., Kumar, V., Gohain, M., Pandey, A., Duvenhage, M.M., Terblans, J.J., Bezuindenhoud, B.C.B., Swart, H.C., 2016. Dopant distribution and influence of sonication temperature on the pure red light emission of mixed oxide phosphor for solid state lighting, Ultrason. Sonochem. 28, 79–89.

Som, S., Das, S., Dutta, S., Visser, H. G., Pandey, M. K., Kumar, P., Dubey, R. K., Sharma, S. K., 2015. Synthesis of strong red emitting Y_2O_3:Eu^{3+} phosphor by potential chemical routes: comparative investigations on the structural evolutions, photometric properties and Judd–Ofelt analysis, RSC Adv. 5, 70887-70898.

Som, S., Kunti, A. K., Kumar, V., Kumar, V., Dutta, S., Chowdhury, M., Sharma, S. K., Terblans, J. J., Swart, H.C., 2014. Defect correlated fluorescent quenching and electron phonon coupling in the spectral transition of Eu^{3+} in $CaTiO_3$ for red emission in display application, J. Appl. Phys. 115, 193101.

Suresh, C., Nagabhushana, H., Darshan, G.P., Basavaraja, R.B., Daruka Prasad, B., Sharma, S.C., Sateesh, M.K., Begumg, J.P.S., 2017, Lanthanum oxyfluoride nanostructures prepared by modified sonochemical method and their use in the fields of optoelectronics and biotechnology, Arab. J. Chem. https://doi.org/10.1016/j.arabjc.2017.03.006.

Tian, Y., Liu, Y., Hua, R., Na, L., Chen, B., 2012. Synthesis and luminescent properties of spindle-like $CaWO_4:Sm^{3+}$ phosphors, Mater. Res. Bull. 47, 59–62.

V. Sharma, A. Das, V. Kumar, 2016, Eu^{2+},Dy^{3+} codoped $SrAl_2O_4$ nanocrystalline phosphor for latent fingerprint detection in forensic applications, Mater. Res. Exp. 3, 015004.

Vijayakumar, M., Marimuthu, K., 2015. Structural and luminescence properties of Dy^{3+} doped oxyfluoro - borophosphate glasses for lasing materials and white LEDs, J. Alloy Compd. 25, 230–241.

Venkatachalaiah, K.N., Nagabhushana, H., Darshan, G.P., Basavaraj, R.B., Daruka Prasad, B., Sharma, S. C., 2017. Blue light emitting $Y_2O_3:Tm^{3+}$ nanophosphors with tunable morphology obtained by bio-surfactant assisted sonochemical route, Spectrochim. Acta A. https://doi.org/10.1016/j.saa.2017.04.033.

Venkatachalaiah, K.N., Nagabhushana, H., Darshan, G.P., Basavaraj, R.B., Daruka Prasad, B., 2017. Novel and highly efficient red luminescent sensor based $SiO_2@Y_2O_3:Eu^{3+}$, M^+ (M^+ = Li, Na, K) composite core–shell fluorescent markers for latent fingerprint recognition, security ink and solid state lightning applications, Sensor Actuat. B-Chem. 251, 310-325.

Venkataravanappa, M., Nagabhushana, H., Daruka Prasad, B., Darshan, G.P., Basavaraj, R.B., Vijayakumar, G.R., 2017. Dual color emitting Eu doped strontium orthosilicate phosphors synthesized by bio-template assisted ultrasound for solid state lightning and display applications, Ultrason. Sonochem. 34, 803–820.

Wang, M. L., Yu, A., Zhu, Y., Yang, M., Mao, C., 2017. Fluorescent nanomaterials for the development of latent fingerprints in forensic sciences. Adv. Funct. Mater. 1606243.

Wang, L., Noh, H. M., Moon, B. K., Park,S. H., Kim, K. H., Shi, J., Jeong, J. H., 2015. Dual-mode luminescence with broad near UV and blue excitation band from $Sr_2CaMoO_6:Sm^{3+}$ phosphor for white LEDs, J. Phys. Chem. C 27, 15517–15525.

Wang J., Heyou H., 2010, Hydrothermal synthesis of high-quality type II CdTe/CdSe quantum dots with near infrared fluorescence, J. Colloid Inter. Sci., 351, 83-87.

Xiao, Q., Zhou, Q., Li, M., 2010. Synthesis and photoluminescence properties of Sm^{3+}doped $CaWO_4$ nanoparticles, J. Lumin. 130, 1092–1094.

Xie, Q., Wang, Y., Pan, B., Wang, H., Su, W., Wang, X., 2012. A novel photocatalyst LaOF: Facile fabrication and photocatalytic hydrogen production, Catal. Commun. 27, 21–25.

Xu, J., Ju, Z., Gao, X., An, Y., Tang, X., Liu W., 2013. $Na_2CaSn_2Ge_3O_{12}$: A novel host lattice for Sm^{3+} doped long-persistent phosphorescence materials emitting reddish orange light, Inorg. Chem. 52, 13875–13881.

Zhang, J. K., Li, Y., Ji, J., Liu, B., 2016. High-resolution and universal visualization of latent fingerprints based on aptamer-functionalized core–shell nanoparticles with embedded SERS reporters, ACS Appl. Mater. Inter. 8, 14389–14395.

Zhang, Y., Li,X., Li, K., Lian, H.,2015. M. Shang, J. Lin, Crystal-site engineering control for the reduction of Eu^{3+} to Eu^{2+} in $CaYAlO_4$: Structure refinement and tunable emission properties, ACS Appl. Mater. Inter. 4, 2715–2725.

Zhu, J., 2005. Shape dependent full width at half maximum of the absorption band in gold nanorods, Phys. Lett. A 339, 466–471.

Zou, X., He, L., Tan, D., Lei, F., Jiang, N., Zheng, Q., Lin, D., Xu, C., Liu, Y., 2017. Anneal-induced transformation of phase structure, morphology and luminescence of $GdPO_4$:Sm^{3+} nanomaterials synthesized by a hydrothermal method, Dalton Trans. 46, 2948-2956.

Zhiguo Xia, Yuanyuan Zhang, Maxim S. Molokeev, Victor V. Atuchin, 2013. Structural and luminescence properties of Yellow-emitting $NaScSi_2O_6$:Eu^{2+} phosphors: Eu^{2+} site preference analysis and generation of Red emission by co doping Mn^{2+} for White-light-emitting diode applications, J. Phys. Chem. C 117 (40), 20847–20854.

Zhiguo Xia, Yuanyuan Zhang, Maxim S. Molokeev, Victor V. Atuchin, Yi Luo, 2013. Linear structural evolution induced tunable photoluminescence in clinopyroxene solid-solution phosphors, Sci. Rep. 3, 3310-3317.

Zhiguo Xia, Ru-Shi Liu, Kuan-Wei Huang, Vadym Drozd, 2012. $Ca_2Al_3O_6F$:Eu^{2+}: a green-emitting oxyfluoride phosphor for white light-emitting diodes, J. Mater. Chem. 22, 15183-15189.

Zhiguo Xia, Maxim S. Molokeev, Aleksandr S. Oreshonkov, Victor V. Atuchin, Ru-Shi Liu, Cheng Dong, 2014. Crystal and local structure refinement in $Ca_2Al_3O_6F$ explored by X-ray diffraction and Raman spectroscopy, Phys. Chem. Chem. Phys. 16, 5952-5957.

Graphical abstract

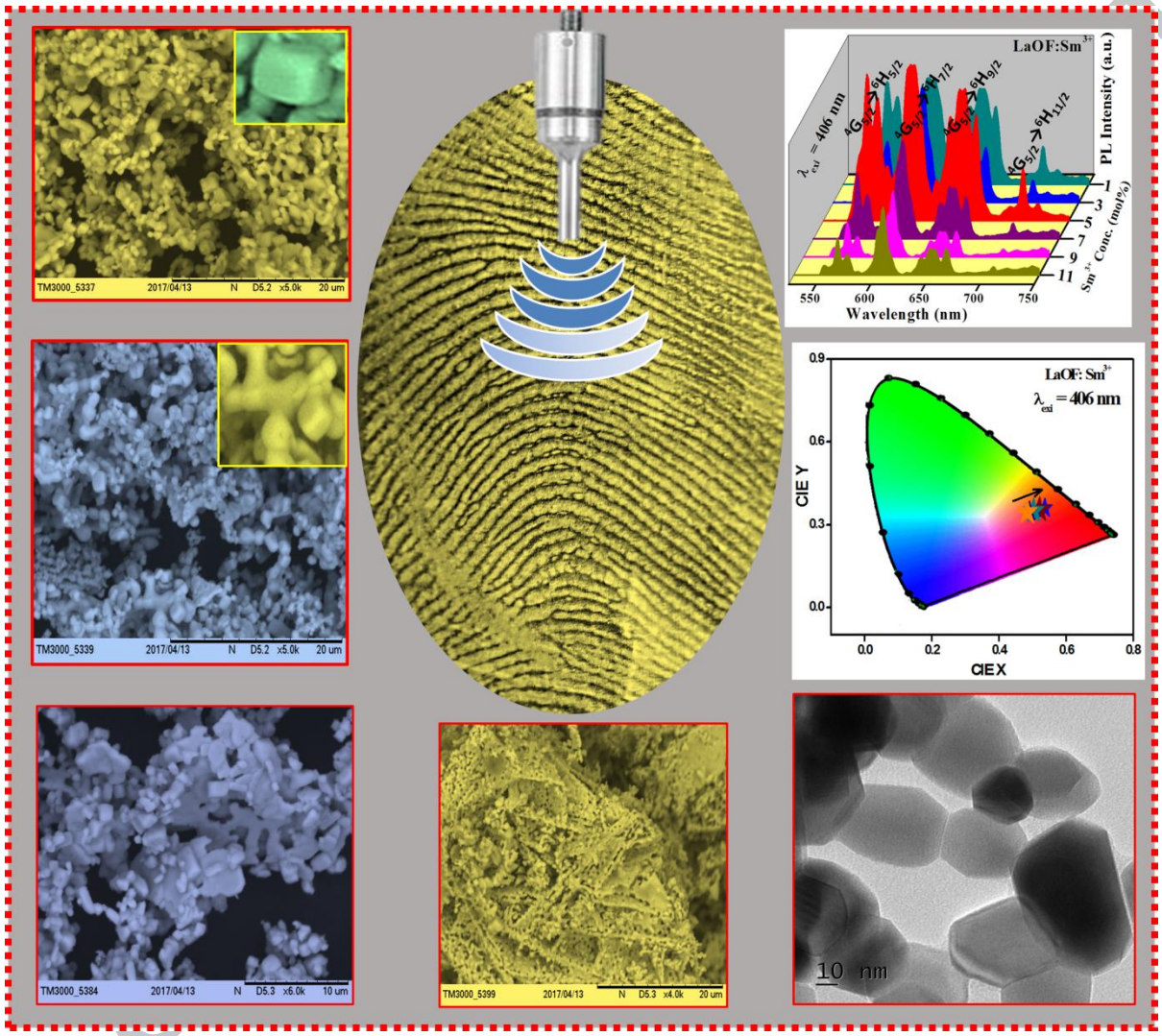

Research highlights

- LaOF: Sm^{3+} nanopowder were prepared using eco-friendly sonochemical route.
- Optimized nanopowder was used as efficient labeling agent for visualization of latent finger print.
- Surface morphologies were studied with different experimental parameters.
- Product was quite useful as fabrication of near ultraviolet white light emitting diodes.

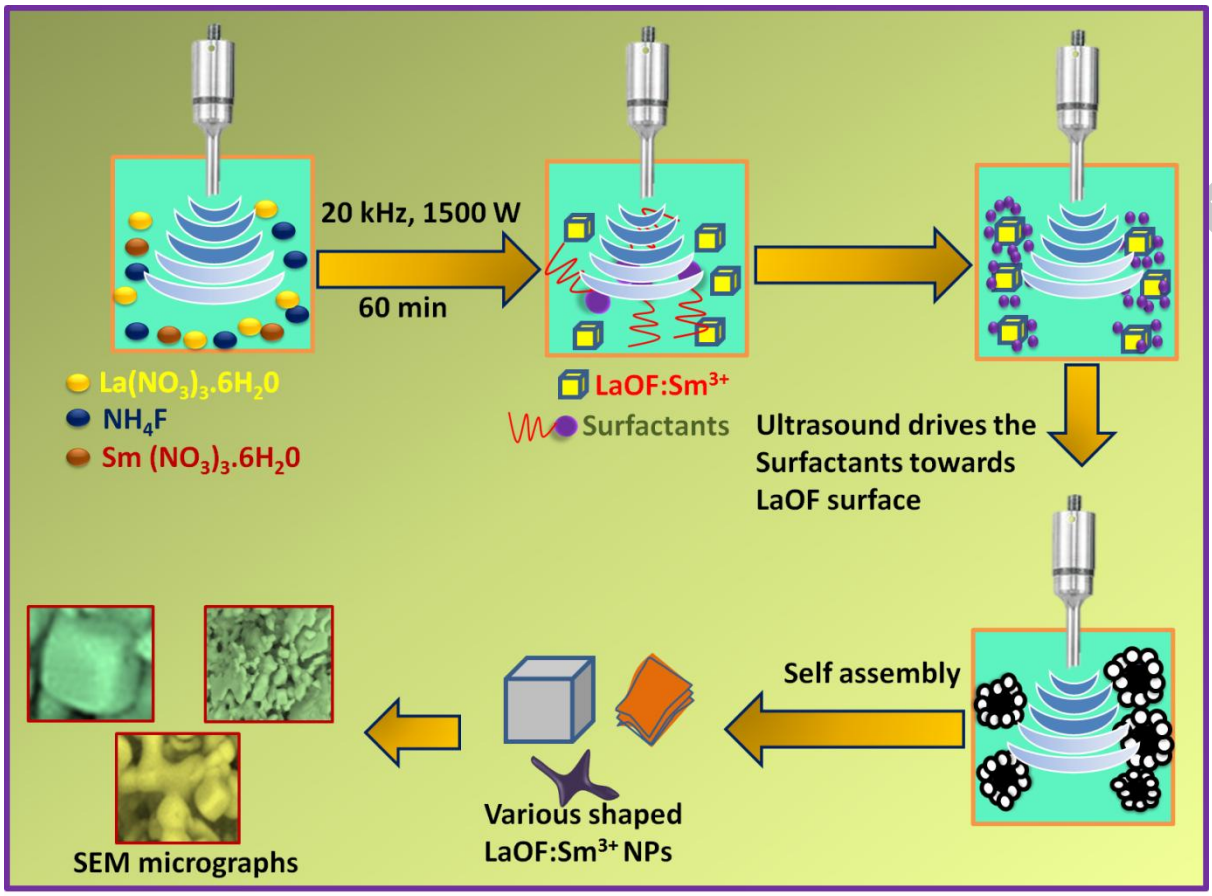

Fig.1. Schematic illustration of ultrasound assisted sonochemical synthesis of LaOF: Sm^{3+} NP.

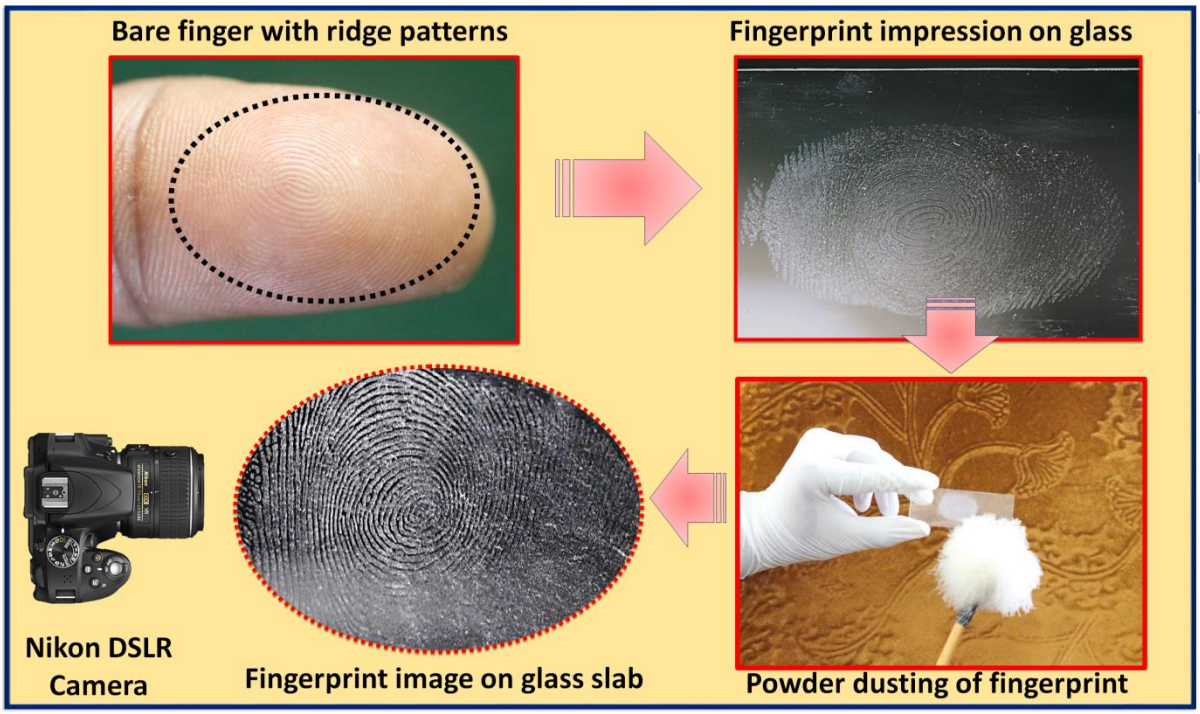

Fig.2. Schematic representation shows visualization of LFPs by powder dusting method.

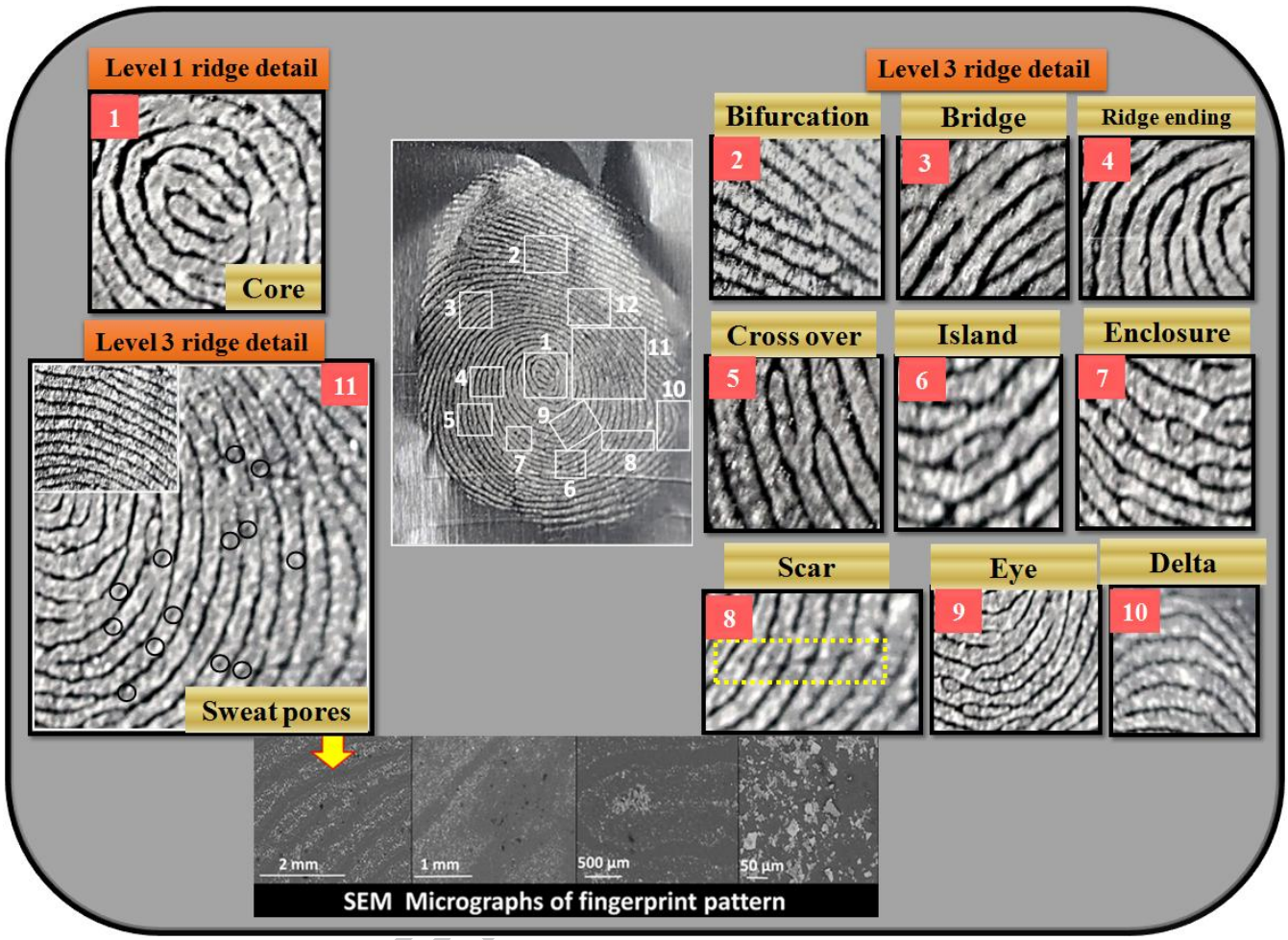

Fig.3. FPs visualized by using LaOF: Sm^{3+} (5 mol %) NP on aluminium foil under normal light and SEM micrographs of ridge patterns. (Highlighted parts clearly displayed the various ridge details).

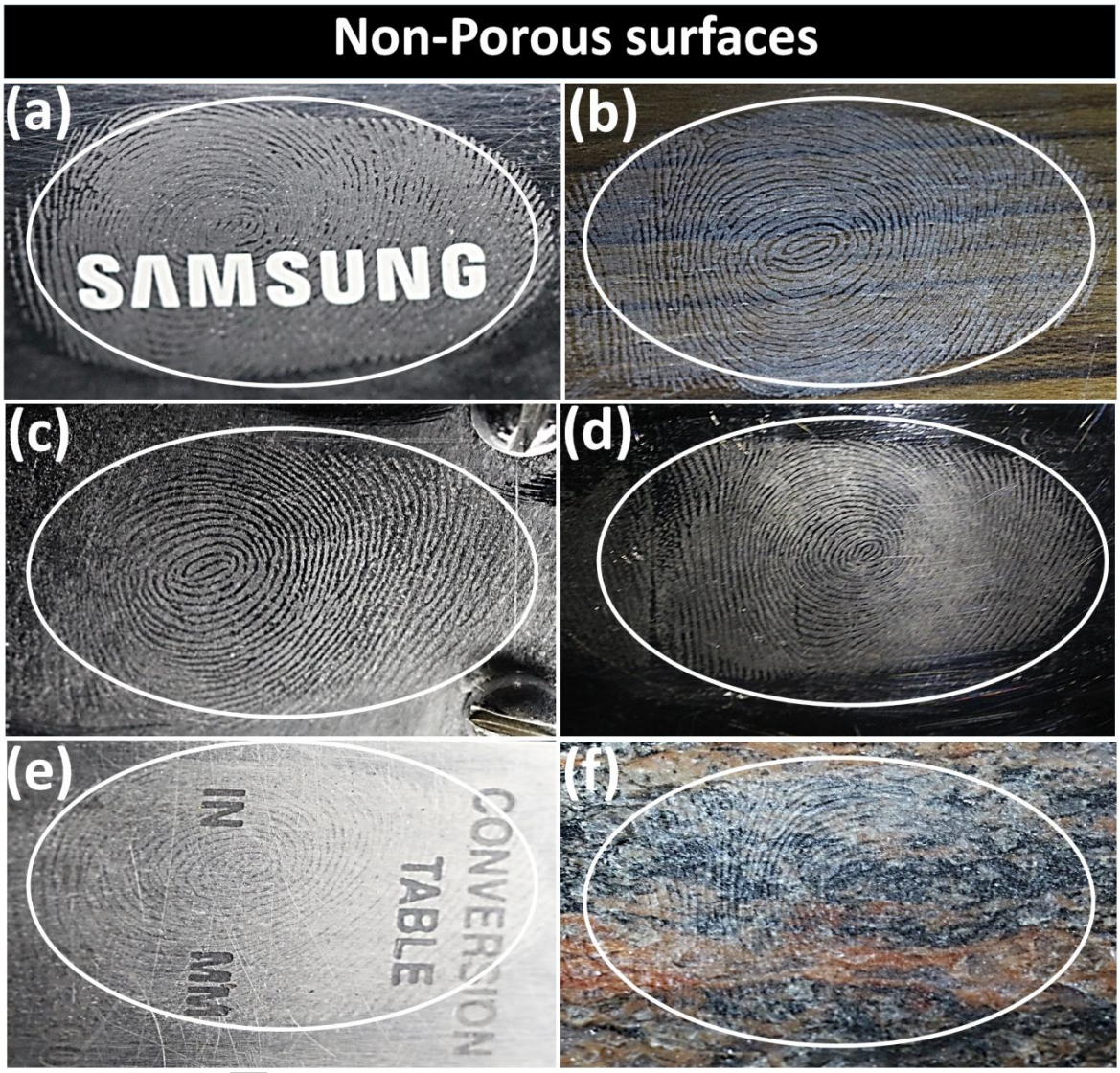

Fig.4. FPs images visualized by LaOF: Sm^{3+} (5 mol %) NP on non-porous surfaces such as (a) remote, (b) wooden sheet, (c) stainless steel, (d) metal shield, (e) metal scale and (f) marble under normal light.

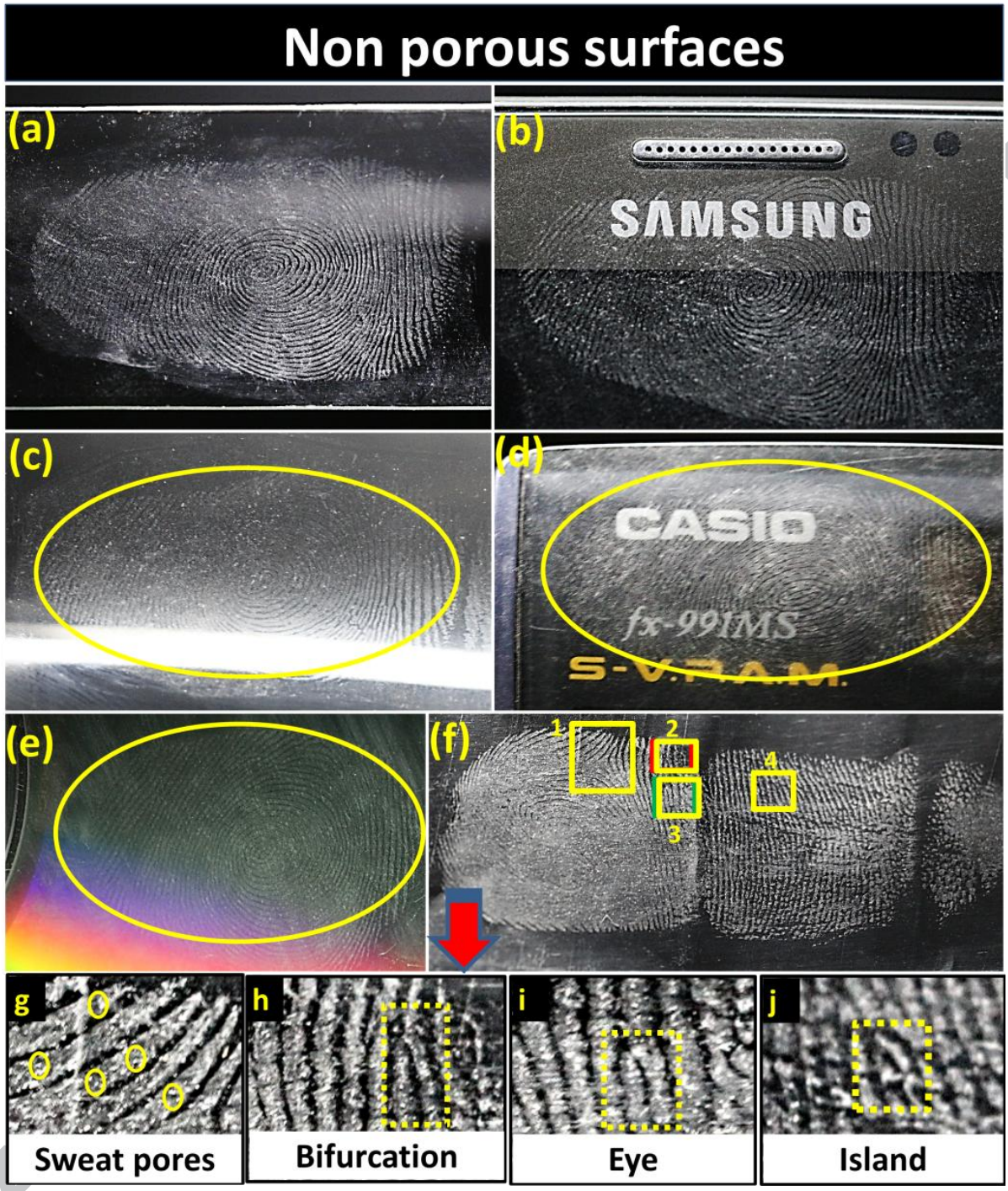

Fig.5. FPs images stained by LaOF: Sm^{3+} (5 mol %) NP on non-porous surfaces namely (a) glass slab, (b) cell phone screen, (c) glass bottle, (d) calculator screen, (e) compact disk, (f) aluminium foil and (g - j) post processed fingerprint exhibits various minutiae ridges (sweat pores, bifurcation, eye and island).

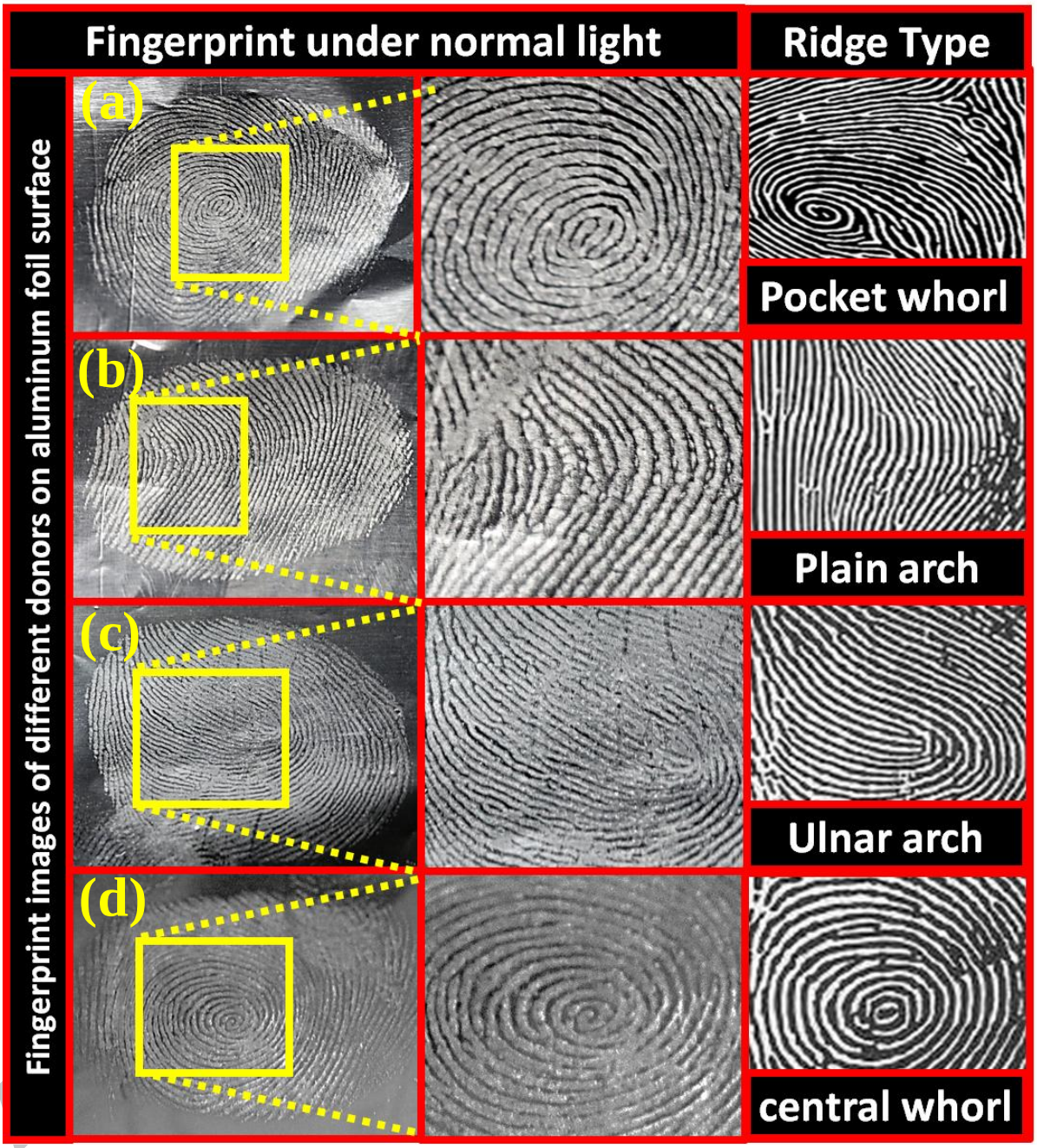

Fig.6. Different donors LFP images on the aluminum foil visualized by using LaOF: Sm^{3+} (5 mol %) NP under visible light. (Right column images show standard ridge patterns).

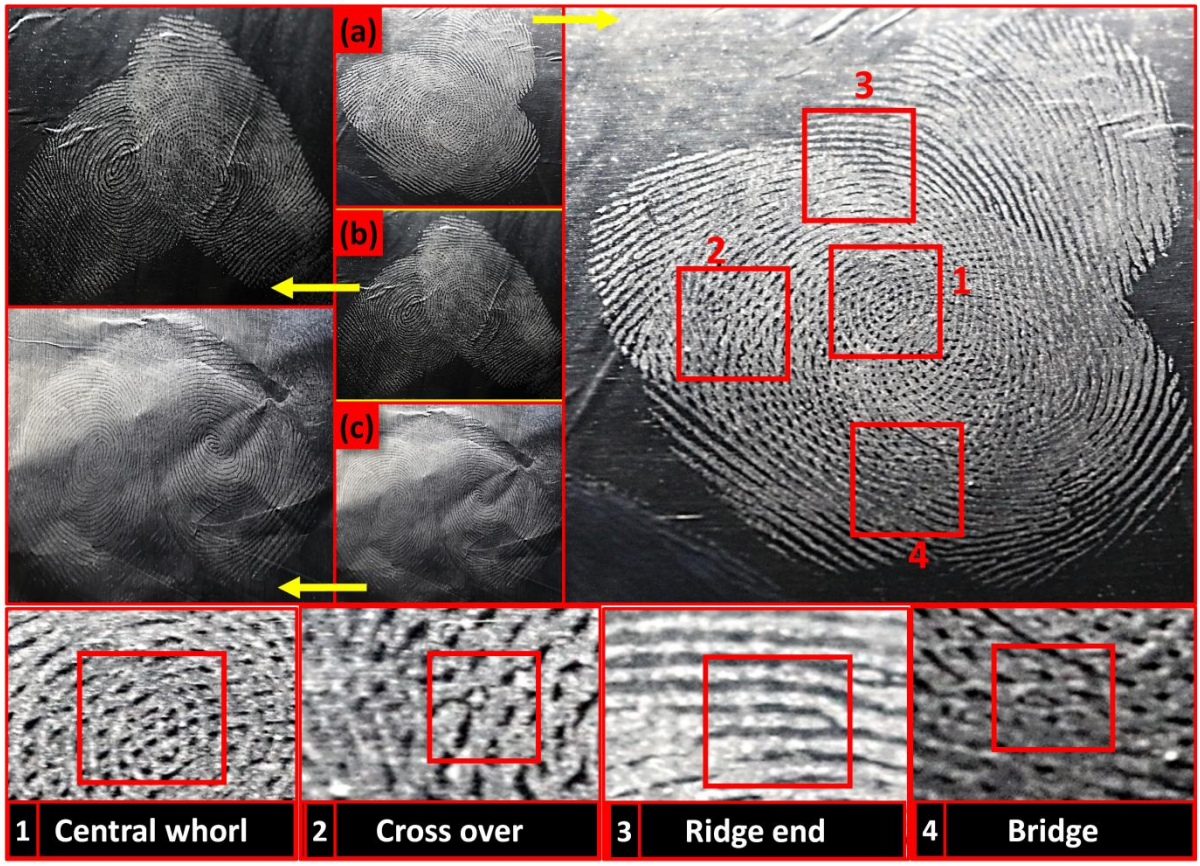

Fig.7. Overlapped LFPs stained by LaOF: Sm^{3+} (5 mol %) NP collected from different donors on the aluminum foil surface under normal light. (Highlighted parts clearly displayed the various ridge details).

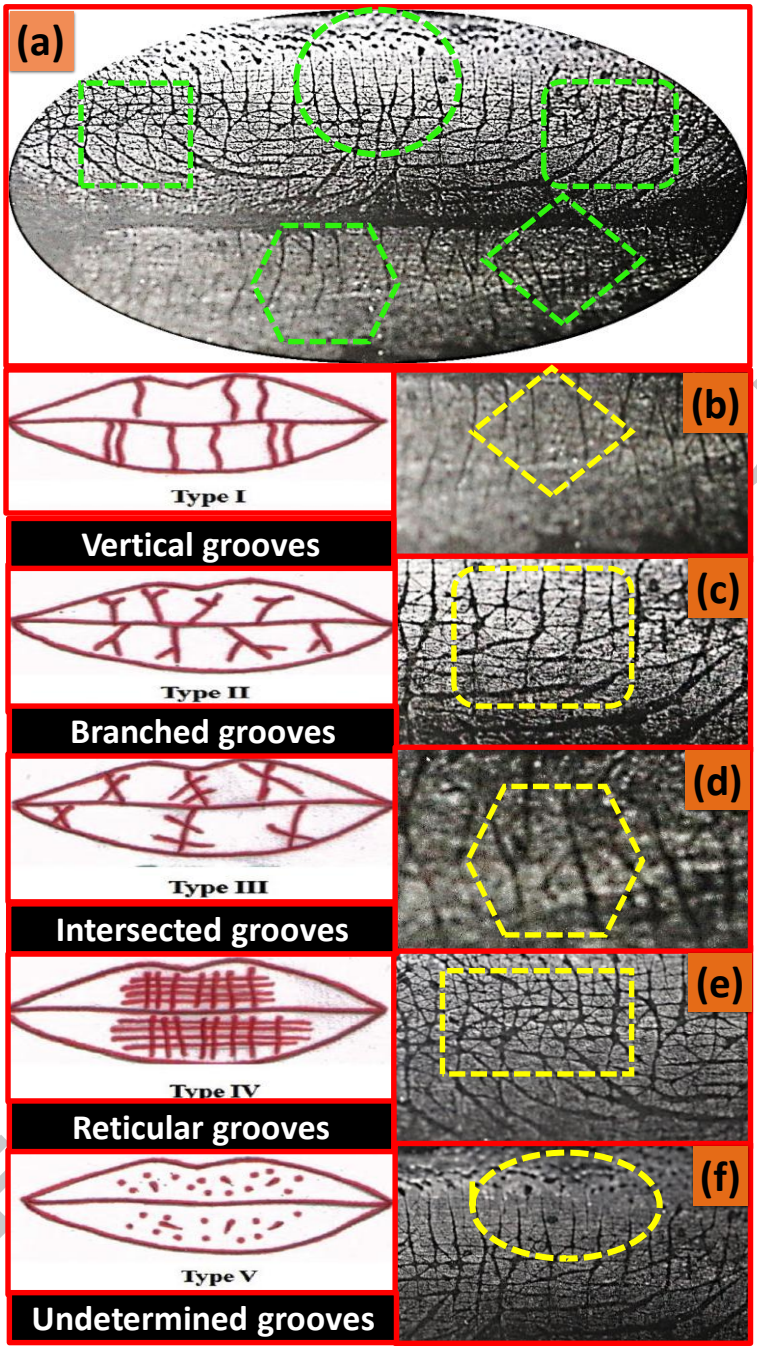

Fig.8 (a) Lips print visualized by LaOF: Sm^{3+} (5 mol %) NP on glass surface and (b-f) various lip print grooves. (Left column images show standard ridge grooves).

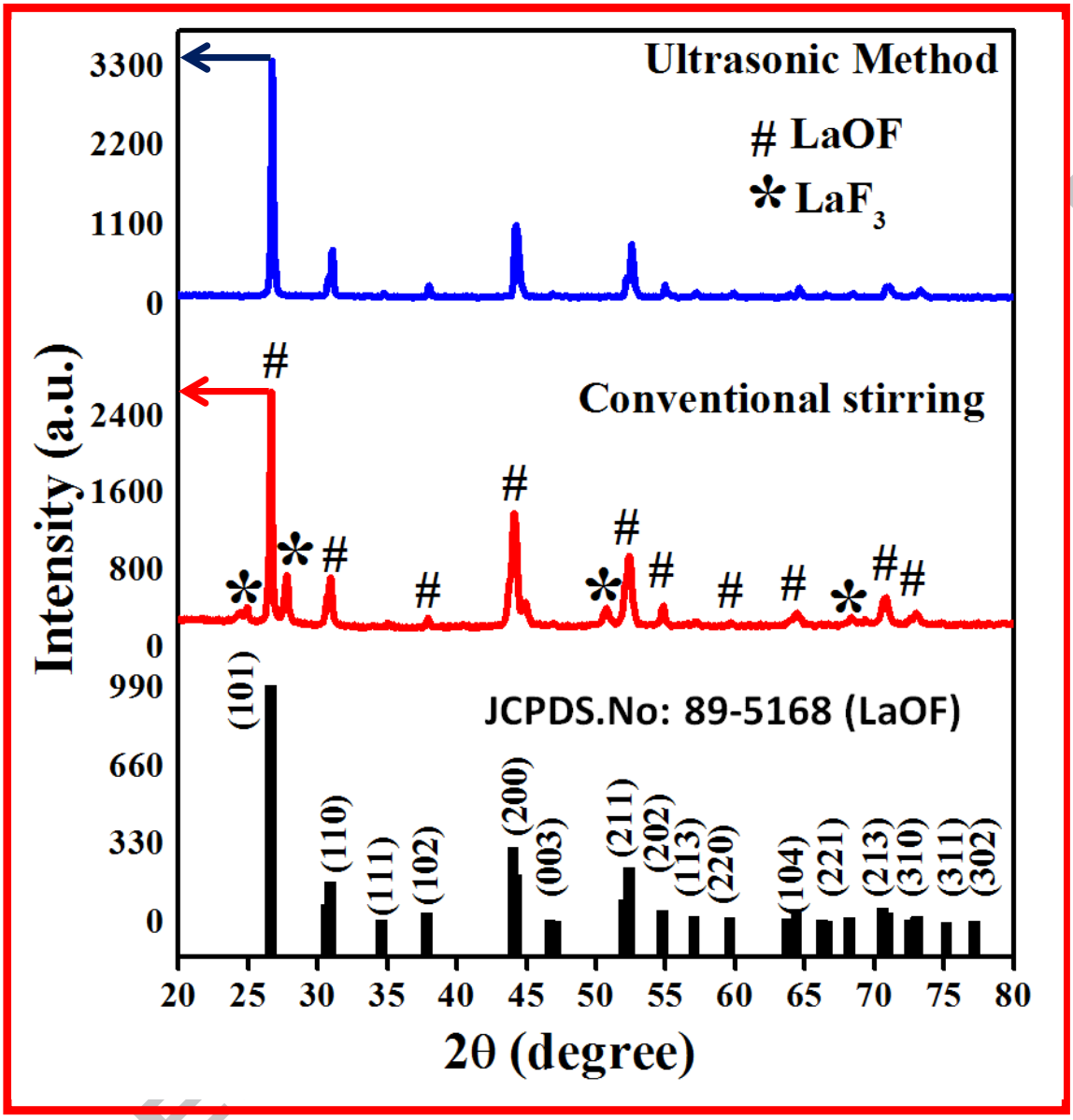

Fig.9. PXRD patterns of LaOF fabricated by (a) conventional stirring and (b) ultrasonication method.

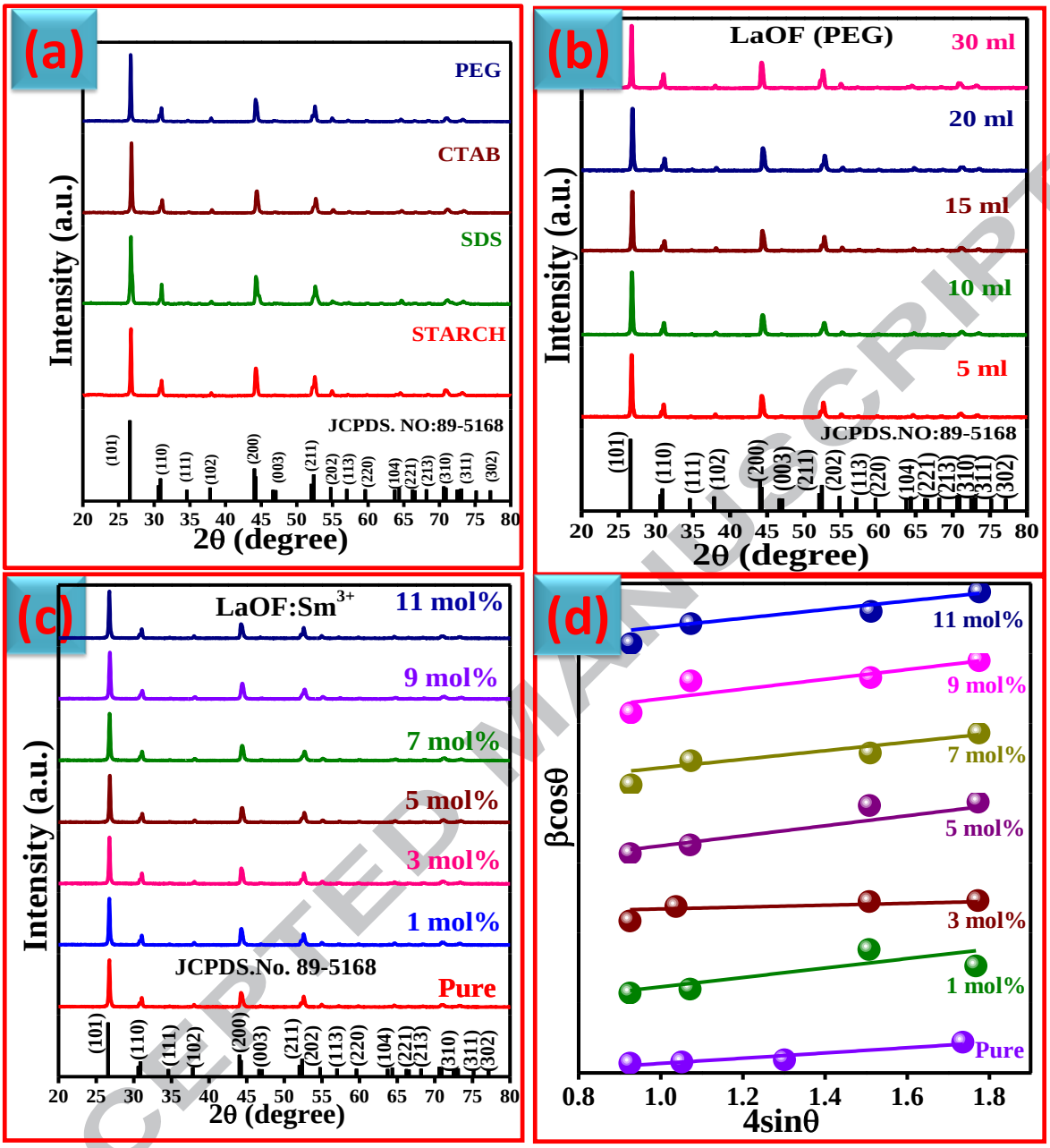

Fig.10. PXRD patterns of LaOF:Sm^{3+} NP synthesized with different (a) surfactants, (b) PEG concentrations, (c) Sm^{3+} (1-11 mol %) and (d) W-H plots of LaOF: Sm^{3+} (1-11 mol %) NP.

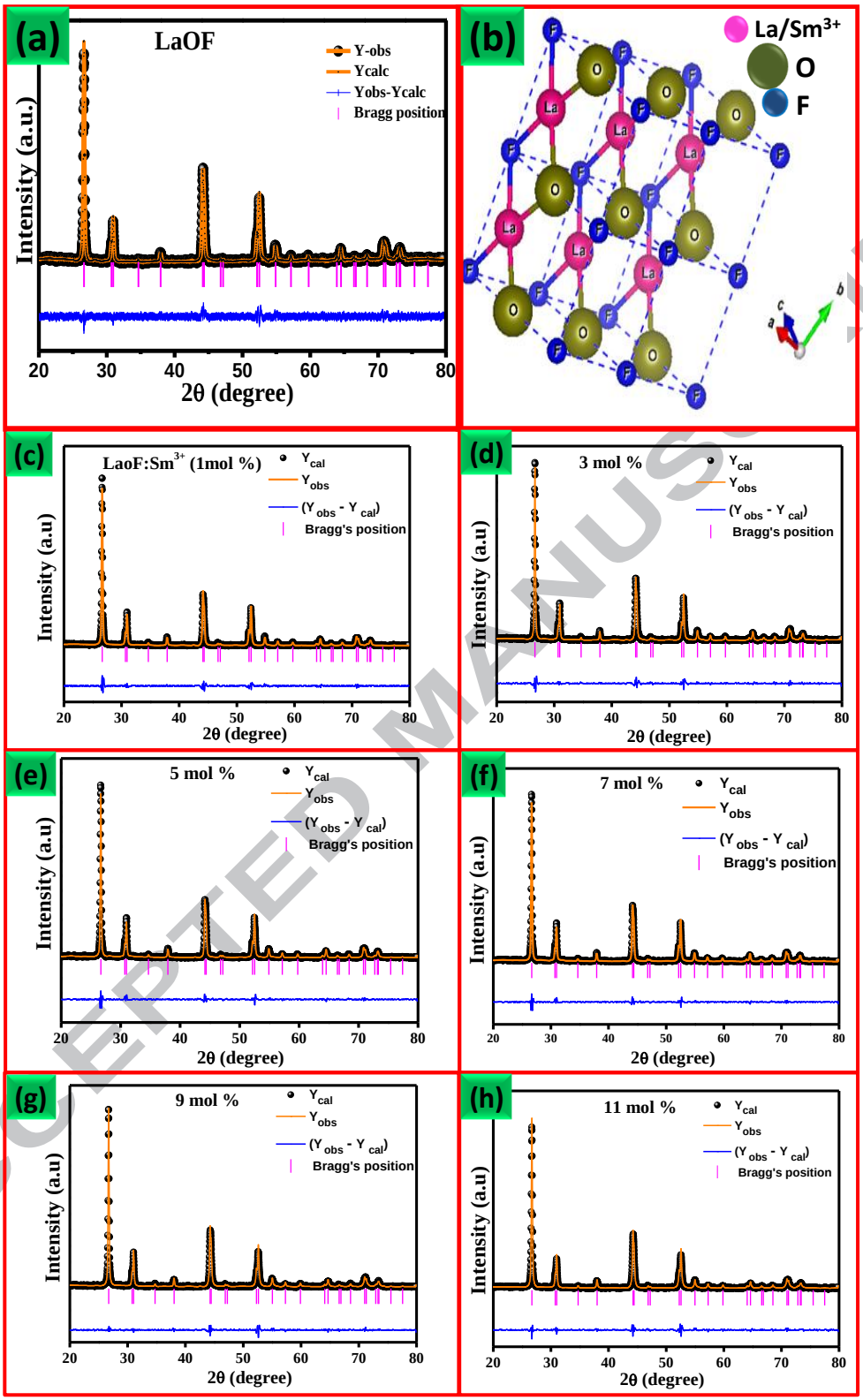

Fig.11. Rietveld refinement of (a) pure LaOF, (c-h) LaOF: Sm^{3+} (1-11 mol %) NP and (b) packing diagram of LaOF: Sm^{3+} (5 mol %) NP.

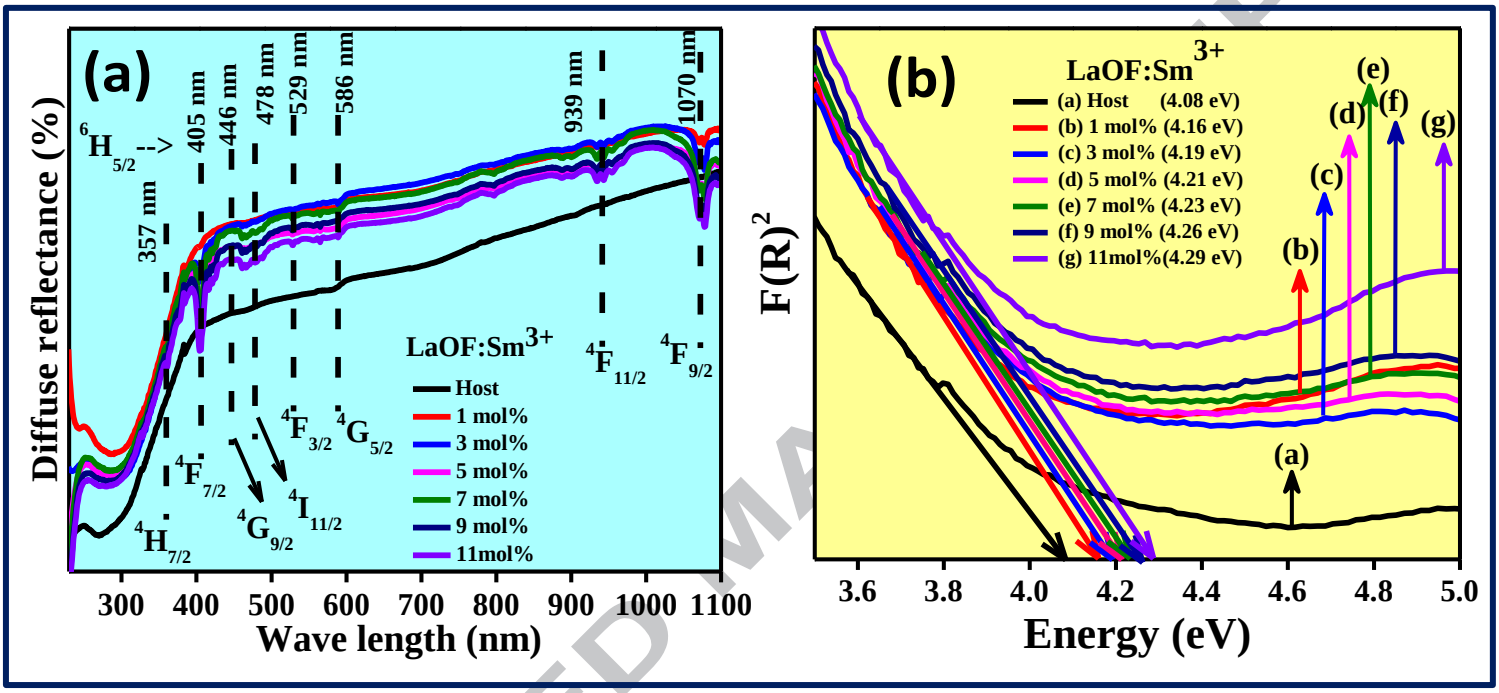

Fig.12 (a) DR spectra and (b) energy band gap spectra of pure & Sm^{3+} (1 -11 mol %) doped LaOF NP.

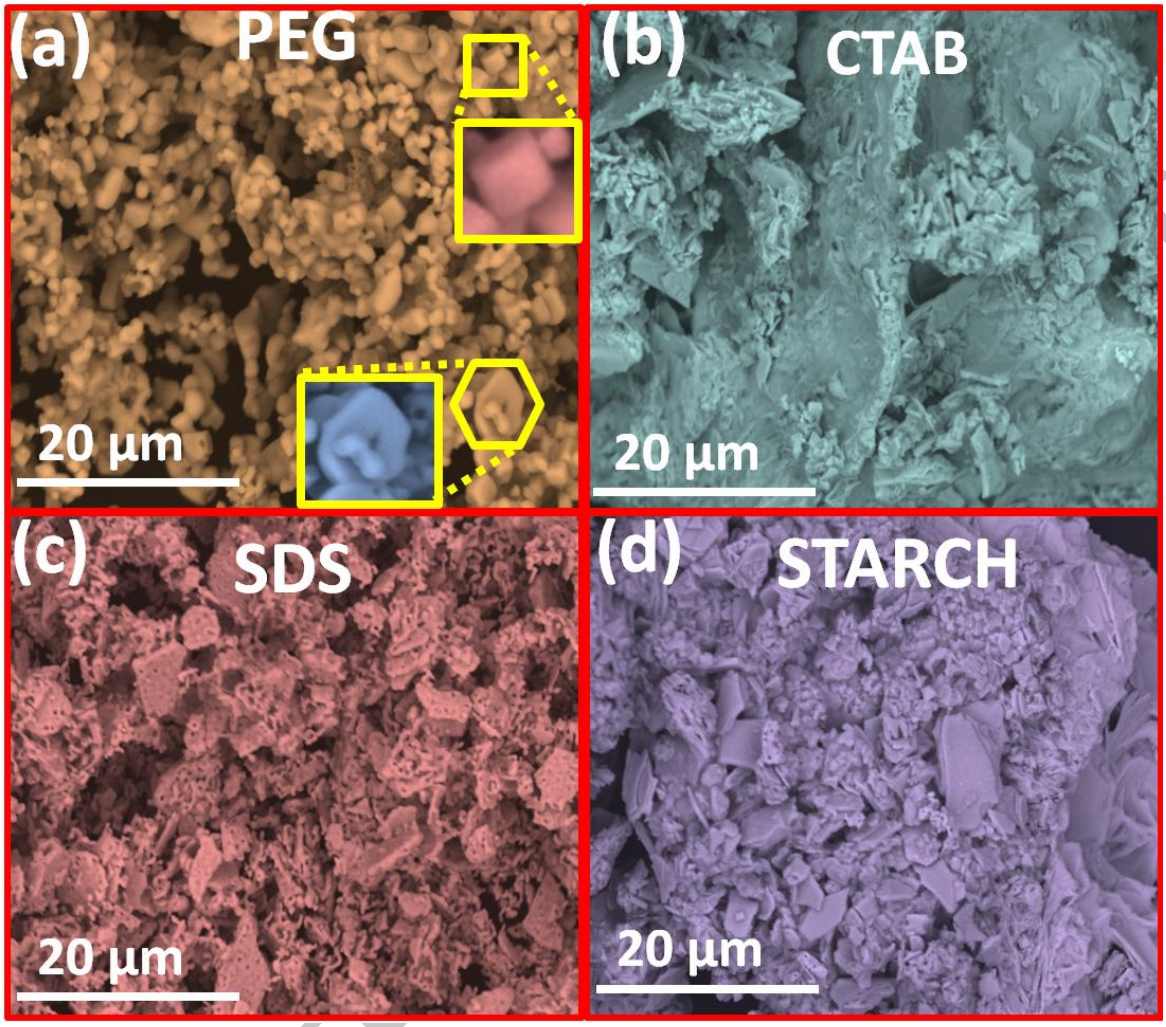

Fig.13. SEM micrographs of LaOF:Sm^{3+} (5 mol %) NP prepared with different surfactants (a) PEG, (b) CTAB, (c) SDS and (d) Starch under 3 h sonication time.

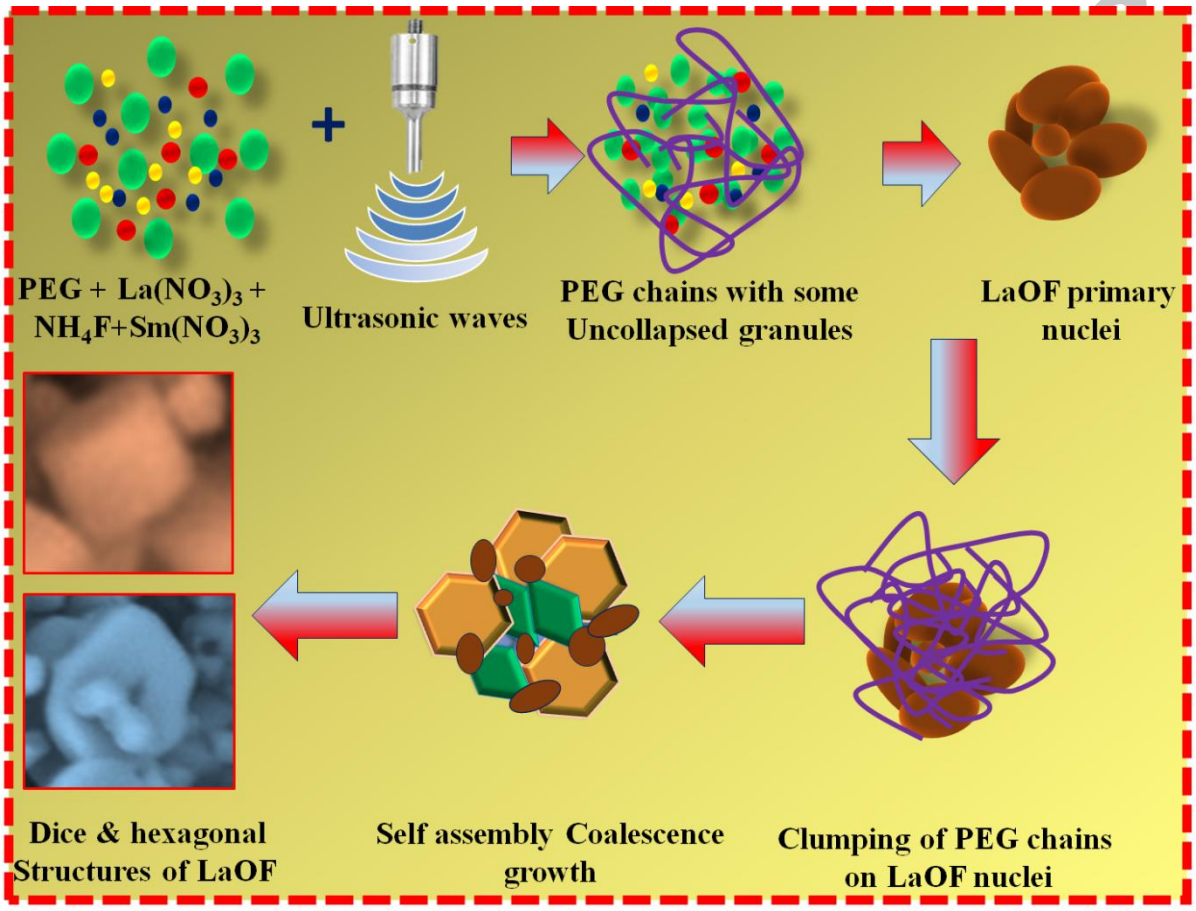

Fig.14. Schematic illustration to show formation mechanism of LaOF: Sm^{3+} (5 mol %) NP in the presence of PEG surfactant.

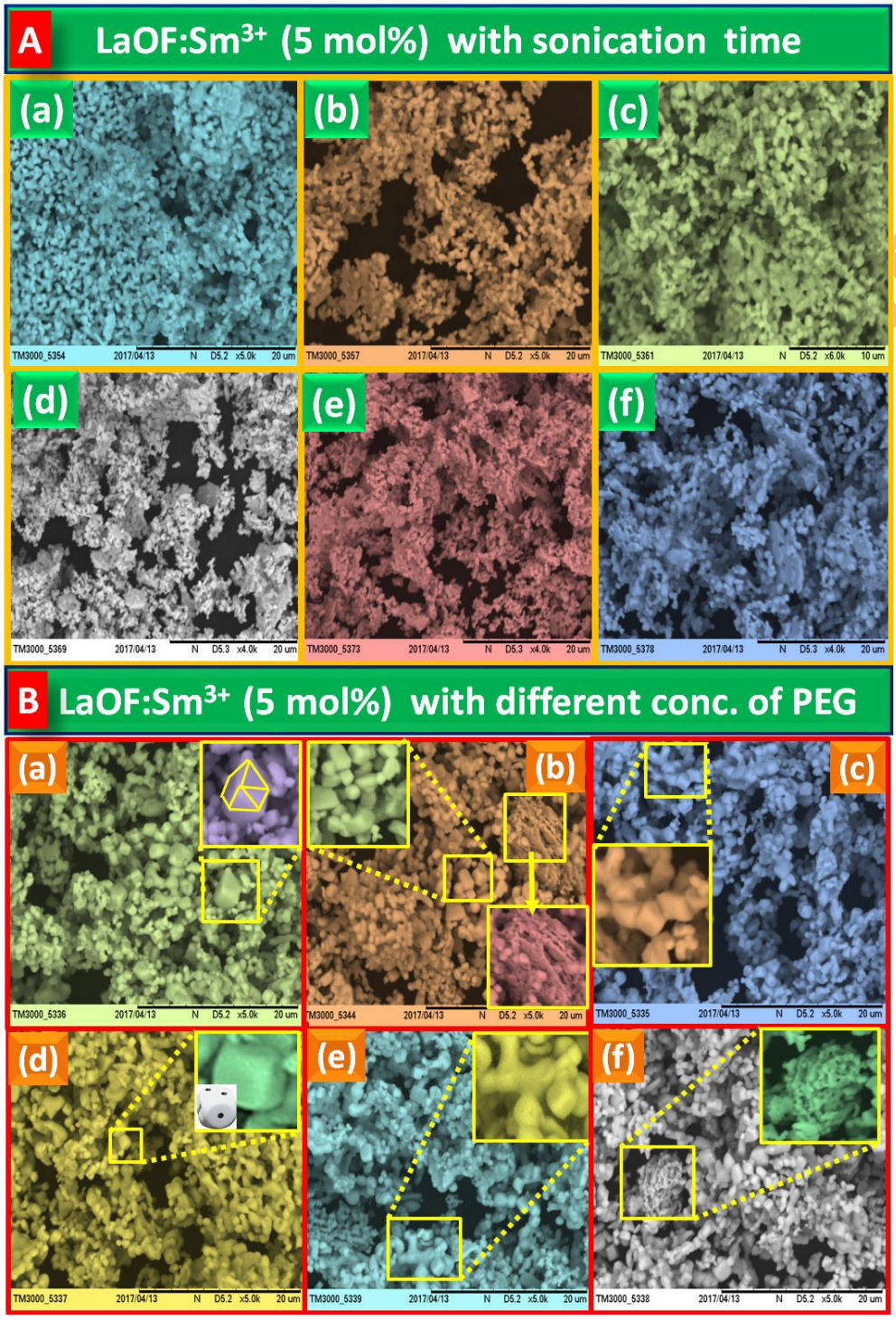

Fig.15. SEM micrographs of LaOF: Sm^{3+} (5 mol %) NP prepared with different (A) sonication time (a) 1 h, (b) 2 h, (c) 3 h, (d) 4 h, (e) 5 h and (f) 6 h with 30 ml of PEG surfactant and (B) concentrations of PEG (a) 5 ml, (b) 10 ml, (c) 15 ml, (d) 20 ml, (e) 25ml and (f) 30 ml with 3 h of sonication time.

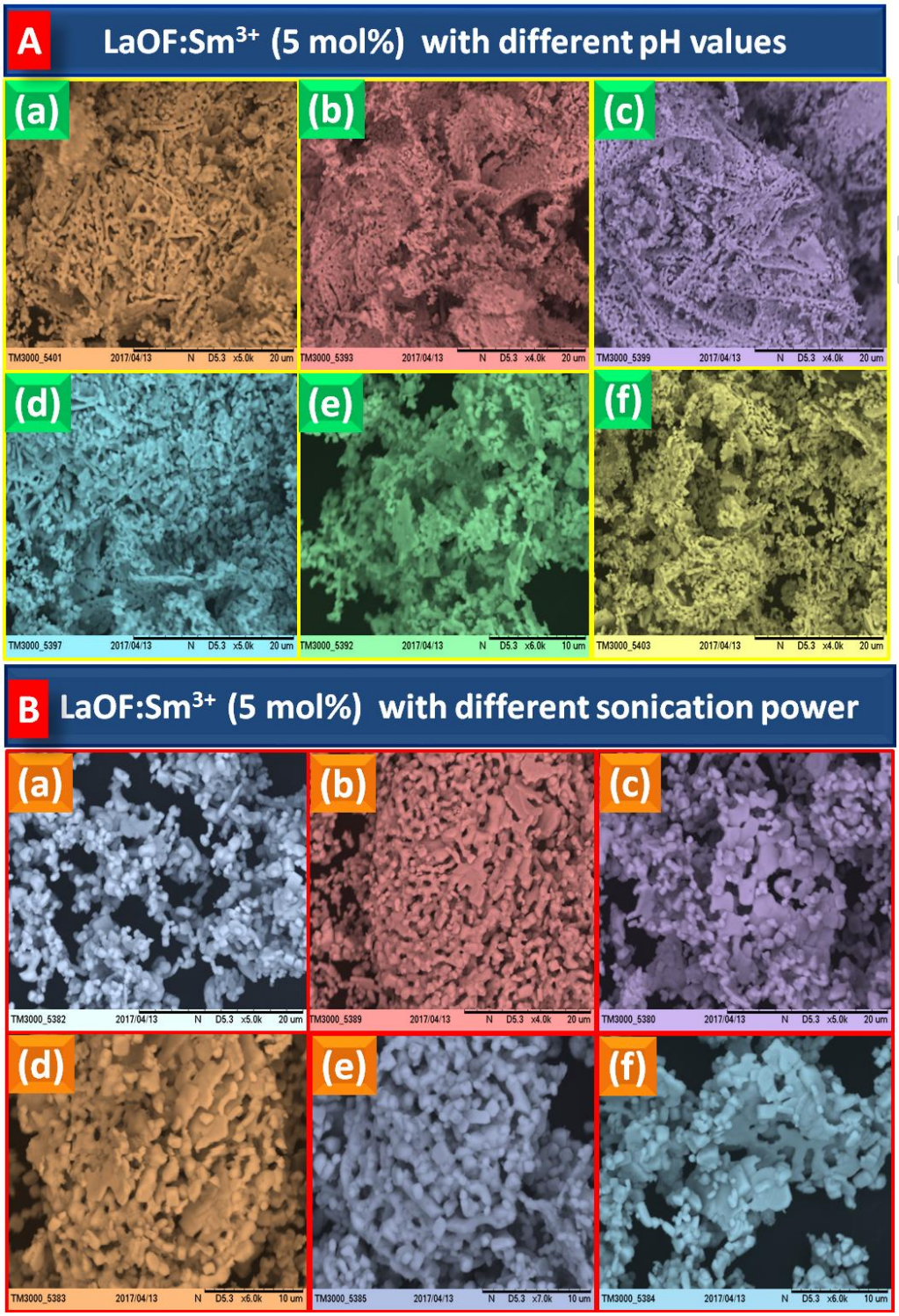

Fig.16. SEM micrographs of LaOF: Sm^{3+} (5 mol %) NP prepared with different (A) pH values (a) 1, (b) 3, (c) 5, (d) 9, (e) 11 and (f) 13 and (B) sonication power (a) 20 kHz, (b) 22 kHz, (c) 24 kHz, (d) 26 kHz, (e) 28 kHz and (f) 30 kHz with 3 h of sonication time and 30 ml of PEG surfactant.

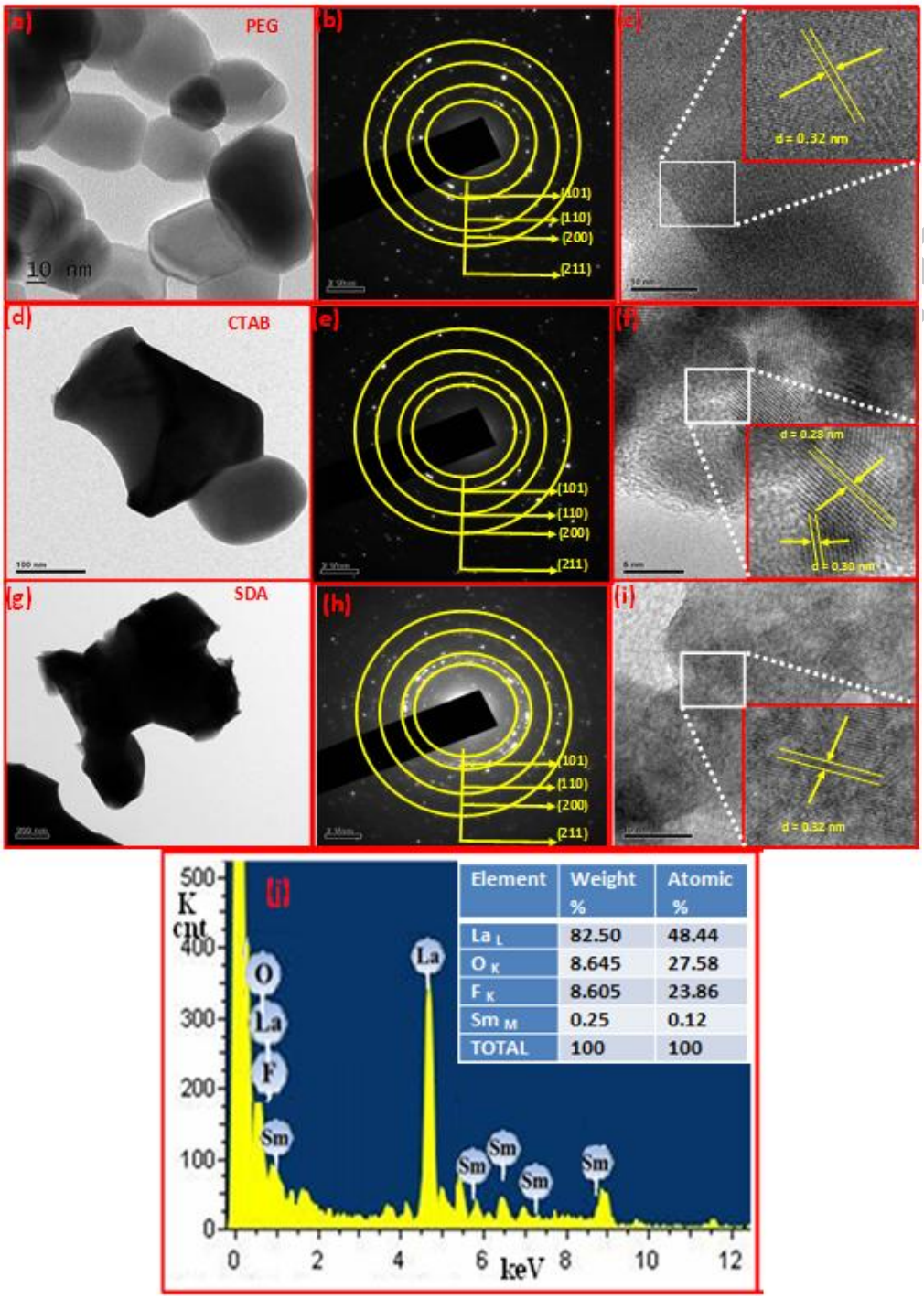

Fig.17 (a, d & g) TEM images, (b, e & h) SAED patterns, (c, f & i) HRTEM images of LaOF: Sm^{3+} (5 mol %) NP prepared with PEG, CTAB and SDS surfactants and (j) EDAX and elemental analysis.

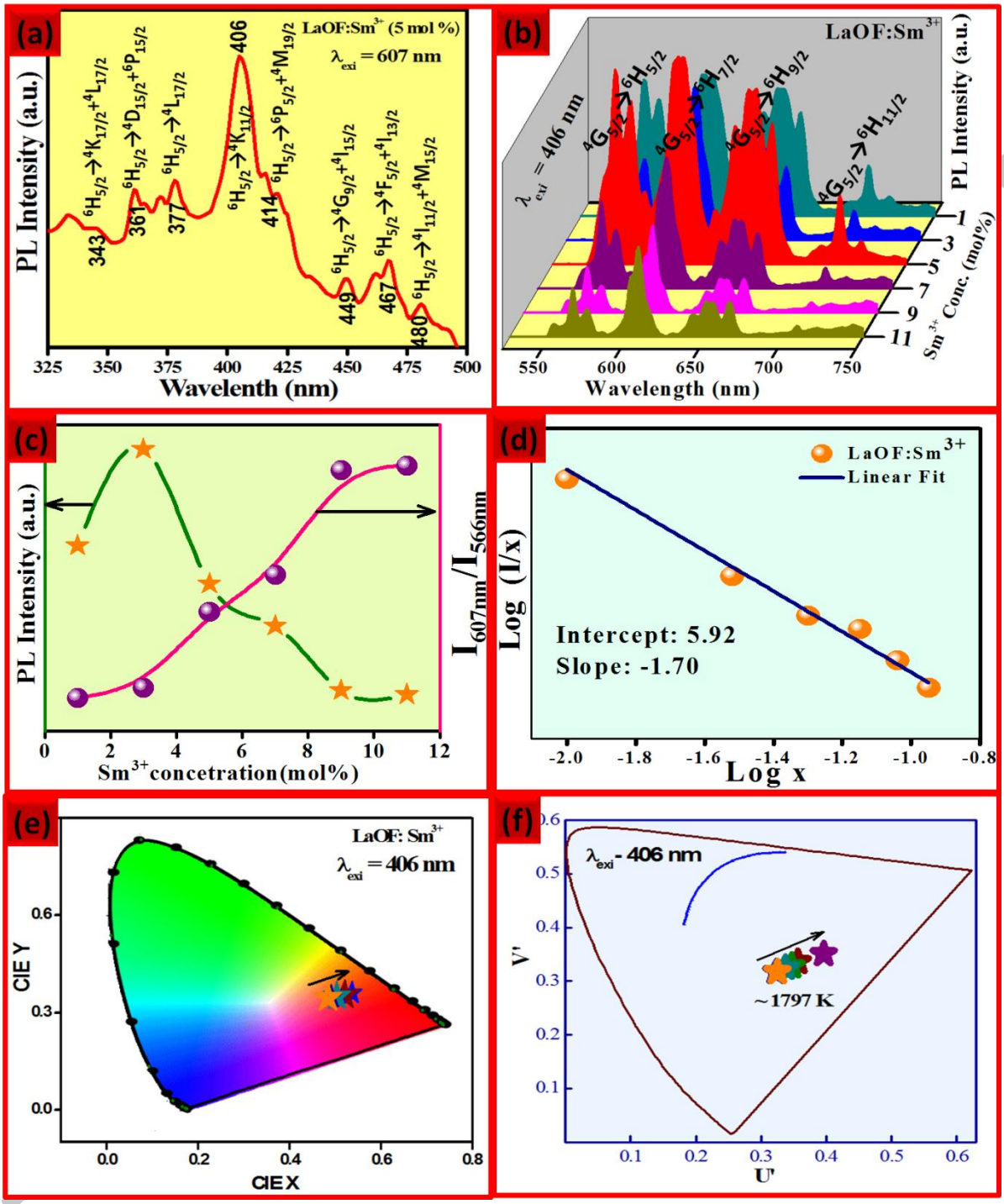

Fig.18 (a) PL excitation (b) Emission spectra (c) Plot of PL emission intensity, asymmetric ratio v/s dopant Sm^{3+} concentration, (d) Logarithmic plot of (I/x) v/s (x), (e) CIE and (f) CCT diagram of LaOF: Sm^{3+} (1-11 mol %) NP prepared with 30 ml PEG under 3 h sonication time.

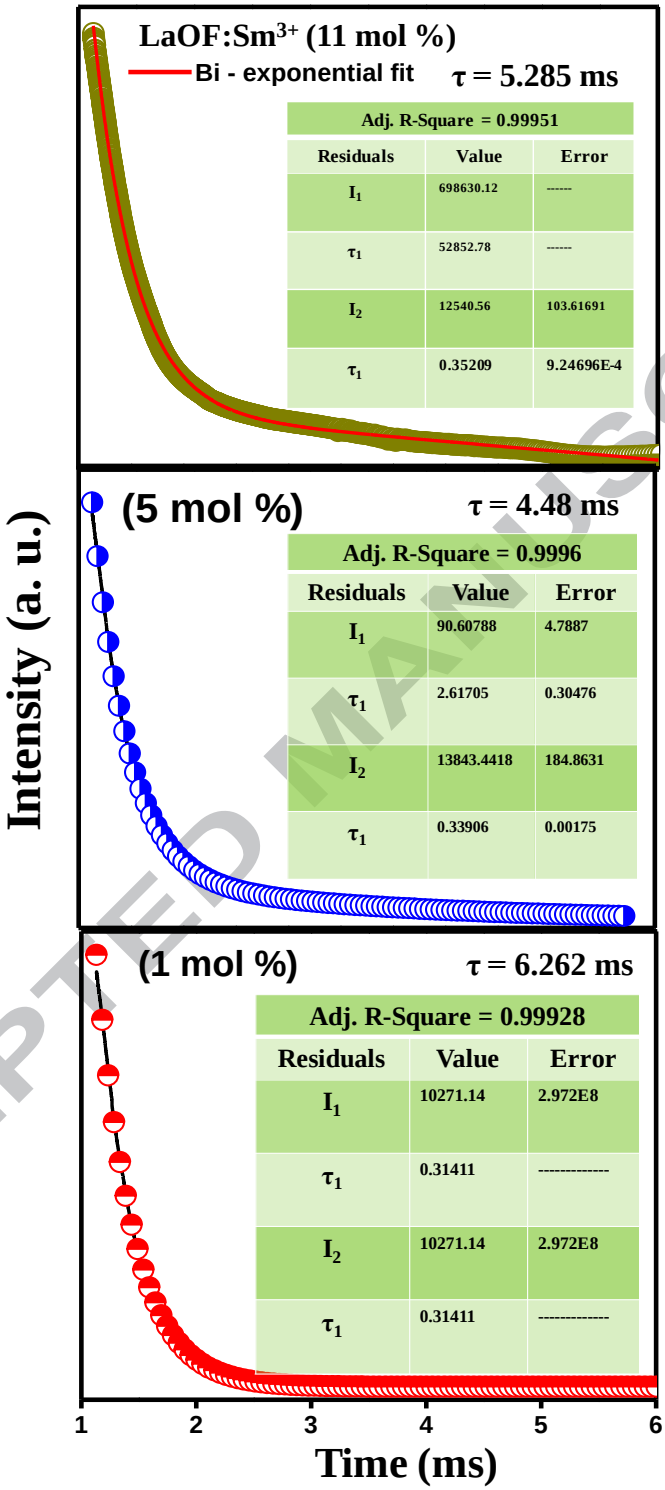

Fig.19. Luminescence decay curve of LaOF: Sm^{3+} NPs.

Table 1: Survey of various important nanomaterials used for the development of FPs.

Sl. No.	Sample	Synthesis technique	Type of luminescence material	Emission Color	References
1	$NaYF_4$:Yb,Er	Solvothermal	Fluorescent	Green	M. Wang et al., 2015
2	$NaYF_4$:Yb,Er/Ce	Hydrothermal	Phosphor	Green	H. Xie et al., 2012
3	$Sr_4Al_{14}O_{25}$: Eu^{2+},Dy^{3+}	Combustion	Phosphor	Blue–Green	V. Sharma et al., 2016
4	ZnO	Solvothermal	Fluorescent	Green	M. J. Choi et al., 2008
5	CdTe/CdSe quantum dots	Hydrothermal	Fluorescent	Blue	J. Wang et al., 2010
6	Eu^{3+}:$Y_2Ti_2O_7$ / SiO_2	Sol–gel method	Phosphor	Red	Saif et al., 2013
7	$YAlO_3$:Tm^{3+}	Combustion	Phosphor	Blue	G. P. Darshan et al., 2016
8	CdTe	Reflux	Phosphor	Multicolor	Cao et al., 2014
9	CdTe-MMT	low-temperature synthesis	Phosphor	Multicolor	F. Gao et al., 2011
10	ZrO_2:Dy^{3+}	Sonochemical	Phosphor	White	Amit et al. 2017
11	LaOF:Sm^{3+}	Sonochemical	Phosphor	Warm orange-red emission	

Table.2. List of chemicals and surfactants used in the present study.

Chemicals	Linear formula	Molecular weight (g/mol)	Details of surfactant			
			Surfactant	Linear formula	Structure	Molecular weight (g/mol)
Lanthanum nitrate	$La(NO_3)_3.6H_2O$	433.01	Starch	$(C_6H_{10}O_5)_n$	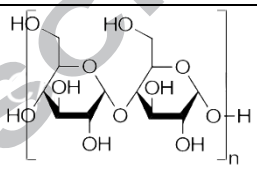	342.30
Ammonium fluoride	NH_4F	37.04	Polyethylene glycol (PEG)	$H(OCH_2CH_2)_nOH$	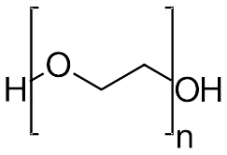	200
Samarium nitrate (III)	$Sm(NO_3)_3.6H_2O$	444.47	Cetrimonium bromide (CTAB)	$CH_3(CH_2)_{15}N(Br)(CH_3)_3$	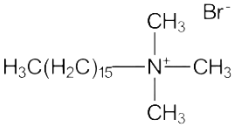	364.45
			Sodium dodecyl sulfate (SDS)	$CH_3(CH_2)_{11}OSO_3Na$	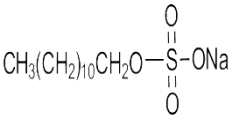	288.38

Table.3. Estimated average crystallite size (D) and micro strain of LaOF: Sm^{3+} NP.

Reaction Parameter		Crystallite size (nm)		Micro strain (x 10^{-3})
		Scherrer's approach	W-H approach	
Surfactant	PEG	19	22	1.25
	Starch	24	28	1.30
	CTAB	36	38	1.36
	SDS	40	42	1.43
PEG (ml)	5	40	43	1.28
	10	37	39	1.31
	15	28	32	1.34
	20	21	29	1.36
	30	18	17	1.39
Sm^{3+} (mol %)	1	49	47	1.31
	3	45	43	1.45
	5	43	41	2.12
	7	41	40	2.23
	9	39	38	2.46
	11	38	36	2.52

Table.4. Rietveld refinement parameter of LaOF: Sm^{3+} (1- 11 mol %) NP.

Compound	LaOF:Sm^{3+}					
Crystal system	Tetragonal					
Space group	P4/nmm					
Hall Symbol	P 4ab 2ab -1ab					
Lattice parameter (Å)	**1mol %**	**3mol %**	**5mol %**	**7mol %**	**9mol %**	**11mol %**
a =b	4.0828 ± 0.004	4.0768 ± 0.002	4.0762 ± 0.006	4.0731 ± 0.009	4.0715 ± 0.002	4.0749 ± 0.007
c	5.8262 ±0.0067	5.8174 ±0.0044	5.8166 ±0.0007	5.8109 ±0.0064	5.8074 ±0.0077	5.8096 ±0.0047
unit cell volume ($Å^3$)	97.121 ±0.00064	97.009 ±0.0005	96.867 ±0.0012	96.765 ±0.0029	96.284 ±0.0007	96.473 ±0.0017
R_p	4.94	4.45	4.41	4.15	3.82	4.06
R_{wp}	6.54	6.06	5.76	5.26	5.09	5.30
R_{exp}	8.13	8.64	8.07	8.16	7.88	8.14
χ^2	0.648	0.491	0.508	0.415	0.417	0.424
GoF	0.80	0.69	0.71	0.64	0.64	0.64
R_{Bragg}	2.62	2.02	2.81	1.53	1.59	1.92
R_F	2.11	2.41	2.51	2.21	2.28	2.00
Density of compound (g/cm^3)	5.947	5.906	5.906	5.906	5.906	5.987

Table.5. J - O intensity parameters (Ω_2 & Ω_4), radiative transition probability (A_T), radiative lifetime (τ_{rad}), branching ratio (β_R), asymmetric ratio (A_{21}), energy gap (E_g) and refractive index (n) of LaOF: Sm^{3+} (1–11 mol %) NP.

Sm^{3+} Conc. (mol %)	**J–O intensity parameters ($\times 10^{-20}$ cm^2)**		**A_T (s^{-1})**	**τ_{rad} (ms)**	**β_R**	**A_{21}**	**Energy gap (eV)**	**Refractive index (n)**
	Ω_2	**Ω_4**						
1	2.32	1.92	342	41	8.96	1.12	4.16	1.837
3	2.56	2.42	292	42	8.93	1.14	4.19	1.837
5	2.34	2.14	278	42	9.91	1.09	4.21	1.838
7	2.48	1.83	284	39	9.96	1.07	4.23	1.838
9	2.49	1.87	321	32	9.96	1.05	4.26	1.838
11	2.18	1.54	308	34	9.98	1.08	4.29	1.841

Table.6. Photometric characteristics of LaOF: Sm^{3+} (1- 11 mol %) NP.

Sm^{3+} (mol %)	**CIE**		**CCT**		**CCT (K)**	**CP (%)**
	X	**Y**	**U_o**	**V_o**		
1	0.5365	0.3591	0.3441	0.5182	1752.44	85.12
3	0.5213	0.3546	0.3356	0.5137	1768.83	84.43
5	0.5121	0.3512	0.3309	0.5106	1784.23	82.34
7	0.5037	0.3502	0.3252	0.5087	1812.73	81.10
9	0.4916	0.3482	0.3174	0.5058	1866.88	80.21
11	0.4846	0.3465	0.3132	0.5038	1903.25	79.48